

Revision 2

Petrogenesis of the Kulyk Lake monazite-apatite-Fe(Ti)-oxide occurrence revealed using in-situ LA-(MC)-ICP-MS trace element mapping, U-Pb dating, and Sm-Nd isotope systematics on monazite.

McFarlane, C.R.M. and McKeough, M.

Department of Earth Sciences, the University of New Brunswick

Abstract

The high-grade metamorphic metasedimentary rocks that comprise the Wollaston Domain, northern Saskatchewan, are host to numerous REE-mineralized pegmatite bodies, including the Kulyk Lake monazite-apatite-Fe(Ti)-oxide occurrence. This occurrence, which is defined by a 3-5cm wide sinuous zone of granoblastic monazite, apatite and titanomagnetite, is enclosed within aplitic monzonite and granitic pegmatite dykes. Monazite in this dyke was studied in detail using *in-situ* laser-ablation inductively-coupled plasma mass spectrometry (LA-ICP-MS) and LA-multi-collector (MC)-ICP-MS. A combination of *in-situ* LA-ICP-MS trace element mapping, trace-element quantification and U-Pb dating were used to identify a significant volume of partial resorbed xenocrystic monazite and zircon cores within the monazite-apatite-Fe(Ti)-oxide zone. This xenocrystic monazite is locally characterized by anomalously high As, V, Mo, and Eu concentrations and high $(La/Yb)_{CN}$ (i.e., >1000) consistent with their derivation from metalliferous black shales. The U-Pb age distribution of the inherited monazite and zircon populations matches that of the middle- to upper-Wollaston Group sedimentary succession. The latter was confirmed by *in-situ* Sm-Nd isotope systematics measured by LA-MC-ICP-MS that

24 yielded $\epsilon\text{Nd}_{(1830\text{Ma})}$ between -5.0 and -5.7 consistent with derivation from Wollaston Group
25 metasediment. The crystallization of ~1830 Ma anatectic overgrowths on xenocrystic cores is
26 indistinguishable from monazite crystallization in the aplitic monzonite dyke hosting the
27 monazite-apatite-Fe(Ti)-oxide bodies. This study reveals the potential importance of
28 metalliferous monazite-rich lithologies in the anatectic zone to these pegmatite-hosted REE
29 occurrences and suggests that entrainment and magmatic segregation mechanisms may have
30 helped to concentrate monazite, apatite, and Fe(Ti)-oxide prior to final emplacement of the
31 aplite-pegmatite dykes. Similar processes may have occurred regionally and in other high-grade
32 metamorphic terrains worldwide that are endowed with metalliferous metasedimentary
33 protoliths.

34 Keywords: monazite, LA-ICP-MS, monazite-apatite-Fe(Ti)-oxide, Trans-Hudson, detrital
35 monazite, *in-situ* geochronology

36

37

Introduction

38 Recent advances in laser ablation inductively coupled plasmas mass spectrometry (LA-ICP-MS)
39 methods applied to *in-situ* analyses for U-Pb geochronology (Petrus and Kamber, 2012), trace-
40 element analysis and trace element mapping (Paton et al., 2011), and Sm-Nd isotope systematics
41 using laser ablation-multi-collector (MC)-ICP-MS (Fisher et al., 2011) allow us to exploit
42 monazite as a geochronometer and petrogenetic tracer at spatial resolutions (~15 μm diameter)
43 nearing the typical excitation volumes of high-voltage electron microbeam microanalytical
44 applications. The LA-(MC)-ICP-MS technique also allows us to routinely analyze elements
45 present at <10 ppm concentrations and measure radiogenic isotope ratios with high precision for
46 geochronological and isotope tracer investigations.

47 This contribution focuses on the *in-situ* application of these LA-(MC)-ICP-MS
48 techniques to the Kulyk Lake monazite-apatite-Fe(Ti)-oxide occurrence. This occurrence is
49 hosted by upper amphibolite to granulite-facies metasedimentary rocks that comprise the
50 Wollaston Domain, within the central Hearne Province of northern Saskatchewan. The region
51 hosts a variety of U-Th \pm REE mineralized veins and pegmatite-hosted dykes. Those associated
52 with granitic dykes, such as the occurrence at Kulyk Lake, are intimately associated with the
53 adjacent pegmatitic to aplitic host rocks and display textures reminiscent of both hydrothermal
54 deposition and igneous crystallization. As a result, the timing of crystallization of these unusual
55 lithologies relative to their pegmatite host, geochemical trends diagnostic of magmatic or
56 hydrothermal deposition processes, and the isotope systematics relevant to reconstructing
57 possible source rocks for these bodies needs to be reconciled with competing models for their
58 origin. Monazite is well-suited to answer these questions because of its robustness as a U-Pb
59 geochronometer (Alagna et al., 2008; Aleinikoff et al., 2006; Bosch et al., 2002; Cherniak et al.,

60 2004; Fitzsimons et al., 1997; Forbes et al., 2007; McFarlane and Harrison, 2006) and Nd isotope
61 tracer (Fisher et al., 2011). Monazite can also crystallize from REE-saturated anatectic melts
62 (Kelsey et al., 2008; Montel, 1993) and can undergo solid-state hydrothermal alteration and
63 recrystallization leading to resetting of U-Pb ages (Seydoux-Guillame et al., 2002; Williams et
64 al., 2011). The trace element chemistry, internal zoning, and stable isotope systematics of
65 monazite may also be used to reveal details of monazite petrogenesis over a broad range of
66 metamorphic *P-T* conditions (Ayers et al., 2006; Breecker and Sharp, 2007; Williams et al.,
67 2007). Integrating textural, geochemical and isotope datasets for monazite can, therefore, help
68 build petrogenetic models to explain the origin of unusual phosphatic rocks and the LA-(MC)-
69 ICP-MS methodologies applied here are particularly well-suited to this goal.

70

Regional geology

71 The Wollaston Domain (Figure 1) is one of several tectonic blocks that comprise the Hearne
72 Province of the Churchill Craton in Saskatchewan (Bickford et al., 1990; Hoffman, 1989;
73 Hoffman, 1990; Lewry and Collerson, 1990). It is comprised of a northeast-trending, tightly
74 folded linear belt containing Archean granitoid rocks preserved in structural domes, and
75 unconformably overlying Paleoproterozoic metasedimentary rocks that were deformed and
76 metamorphosed during the Trans Hudson Orogeny (Lewry and Sibbald, 1980; Tran and Yeo,
77 1997). Partial melting during granulite-facies metamorphism of the Wollaston Group
78 supracrustal rocks produced migmatitic paragneisses and anatectic granitic rocks that are
79 constrained to the latter stages of Trans-Hudson deformation (Annesley et al., 2005; Bickford et
80 al., 1990; Bickford et al., 2005; Chiarenzelli, 1989; Chiarenzelli et al., 1998; Yeo and Delaney,
81 2007).

82 The Wollaston Group supracrustal rocks in the Kulyk Lake region overly Archean
83 granites that range between 2650 Ma and 2500 Ma based on U-Pb zircon thermal ionization
84 mass spectrometry (TIMS) analyses (Annesley et al., 1992; Annesley et al., 2005; Ray and
85 Wanless, 1980; Rayner et al., 2005). A detailed study by Tran et al. (2010) described the
86 regional volcano-sedimentary stratigraphy of the Wollaston Group and established the relative
87 contributions from Archean and Paleoproterozoic detritus using whole-rock Sm-Nd data and
88 detrital zircon analyses. The metasedimentary cover at Kulyk Lake (McKeough et al., 2010) is
89 described as a Paleoproterozoic syn-rift passive margin and foreland sequences (Tran et al.,
90 2003; Tran et al., 2008): they are divided into Lower and Upper subgroups that are separated by
91 a regional unconformity. The lower succession includes a basal graphitic pelitic unit overlain by,
92 and in part interleaved with, arkose, conglomerate, quartzite, and calcareous sedimentary rocks.
93 The upper part of the succession includes conglomerates, immature arkosic rocks and calcsilicate
94 rocks and is thought to represent subsequent infilling of a foreland basin. The provenance of
95 these metasedimentary sequences falls into three main zircon populations including: 1) >2400
96 Ma grains that represent detritus shed from the neighbouring Hearne craton; 2) 2100 Ma
97 components thought to represent reworking of syn-rift volcanic rocks, and; 3) 1920-1880 Ma
98 detritus shed from advancing volcanic arc terrains of the western Churchill Province (Su et al.,
99 2012). The lower succession of the Wollaston Group appears to have detritus sourced primarily
100 from Archean protoliths (2600 to 2850 Ma) with locally minor Paleoproterozoic (~2400 Ma)
101 input. In contrast, the middle and upper successions contain significant Paleoproterozoic
102 components (2100 to 1880 Ma) and only minor Archean detritus (Hu et al., 2011).

103 The Paleoproterozoic metasedimentary gneisses are intruded by north-, east- and east-
104 northeast-trending, variably radioactive leucogranite dykes, sills and lenses (Mawdsley, 1957;

105 McKeough and Lentz, 2011; McKeough et al., 2010). U-Th-REE mineralization in the Kulyk
106 Lake area is primarily fracture-controlled within prospective folded and faulted rocks of the
107 basal Wollaston sequences, particularly in the leucogranitic pegmatite dykes that intrude the
108 metasedimentary rocks and locally along the contacts between the host gneisses and pegmatite
109 intrusions. Previous geochronological studies on syn-tectonic diatexite, amphibolite, and
110 numerous foliated and cross-cutting ‘Hudsonian’ granite plutons that intrude the Wollaston
111 group reveal a prolonged history of Trans-Hudson metamorphism, anatexis, and pegmatite and
112 aplite emplacement between ~1840 and ~1770 Ma (Hou et al., 2012). The onset of partial
113 melting under granulite-facies conditions and the generation of restitic diatexitic gneisses
114 occurred between 1840 to 1830 Ma in response to crustal thickening in the domain (Annesley et
115 al., 2005). Emplacement of Hudsonian granitoid rocks peaked between 1830 and 1815 Ma
116 following the initiation of exhumation and decompressional melting. The final transpressional
117 stages of Trans-Hudson orogenesis involved strike-slip deformation, emplacement of
118 undeformed 1780-1760 Ma granitic pegmatite bodies that cross-cut the regional gneissic fabrics,
119 followed by rapid cooling. The Wollaston Group rocks were near or at the surface by 1650 Ma
120 when mature quartz-rich sediments at the base of the Athabasca basin were deposited (Hou et al.,
121 2012).

122 **Description of the occurrence**

123
124 The Kulyk Lake monazite-apatite-Fe(Ti)-oxide occurrence was first described by Watkinson &
125 Mainwaring (1976). The deposit occurs within northeast-striking and steeply southeast dipping
126 upper amphibolite- to granulite-facies calc-silicate paragneisses with assemblages comprised of
127 biotite-hornblende-clinopyroxene-quartz-K-feldspar-plagioclase with variable biotite/hornblende

128 and local magnetite-bearing zones. Psammitic gneisses to the east and west of the calc-silicate
129 gneiss hosting the deposit also contain abundant concordant and locally cross-cutting pegmatitic
130 bodies and granitic sheets.

131 The area of granitoid dykes hosting the monazite-apatite-Fe(Ti)-oxide zone is located
132 ~65 m east of Kulyk Lake (Figure 1b). This zone of granitoid dykes is sub-vertical and ~15 m in
133 length, locally extending as lenses discordant to the north-northeast strike of the regional fabric
134 observed in the adjacent calc-silicate gneisses. The host intrusive unit ranges from granitic
135 pegmatite to monzonitic aplite, with the monazite-apatite-Fe(Ti)-oxide mineralization distributed
136 primarily within the 10-15cm wide aplitic phase of the dyke system. The aplitic monzonite
137 displays a seriate to locally porphyritic texture with a hypidiomorphic granular groundmass of
138 0.2 to 0.5mm perthitic K-feldspar, plagioclase, and minor (<5%) interstitial quartz. Grain
139 boundaries in the groundmass are sutured and locally blurry and are typical of dynamically-
140 recrystallized rocks. Monazite, apatite, and Fe(Ti)-oxide are ubiquitous accessory minerals in
141 the aplitic monzonite and together comprise ~1% modal abundance in thin section. The Fe(Ti)-
142 oxide mineral in the monzonite displays micron-scale exsolution lamellae of rutile and ilmenite.
143 Larger 2 to 4 mm phenocrysts of perthitic K-feldspar host inclusions of subhedral to oval
144 monazite, euhedral to subhedral apatite, and ovoid Fe(Ti)-oxide.

145 The phosphate-rich zone was emplaced along the central part of the host monzonite aplite
146 dyke, and forms concordant but locally tortuous contacts with it (Figure 2a). It is comprised of
147 0.5 to 5cm thick bands of granoblastic fine- to medium-grained reddish brown monazite, pinkish
148 to beige apatite, and an Fe(Ti)-oxide component of medium- to coarse-grained titanomagnetite.
149 The titanomagnetite is typically disseminated throughout the monazite-apatite bands, but may
150 also form as a thick outer rind surrounding monazite-apatite in sharp contact with the aplitic

151 phase of the granitic dyke. The phosphate minerals comprise 70 to 90% of these zones. It is
152 important to note that quartz is absent in the phosphatic zones and only trace amounts of feldspar
153 have been encountered. The monazite-apatite-Fe(Ti)-oxide zone also locally forms lobate
154 embayments or injections into the adjacent monzonitic aplite dyke giving rise to textures
155 reminiscent of magma mingling. These lobate domains are characterized by stromatic Fe(Ti)-
156 oxide layers rimmed by narrow monazite-rich selvages that separate an apatite-rich inner zone
157 from the host aplite dyke. In other parts of the monazite-apatite-Fe(Ti)-oxide occurrence,
158 alternating monazite-rich and apatite-rich bands and schlieren give the zone a layered appearance
159 with no obvious differentiation (Figure 2b). A reddish earthy hematite alteration affected the
160 monazite-apatite-Fe(Ti)-oxide occurrence and the adjacent aplitic and pegmatitic wall rocks.

161 McKeough & Lentz (2011) have also shown that the aplitic monzonite dyke hosting the
162 phosphate zone is also enriched in Nb, Y, REE, U, Th and Zr (NYF-type) albeit at lower
163 absolute concentrations. The monazite-rich zone and its host monzonite dyke also display
164 similar trace element fractionation trends including sub-parallel Chondrite-normalized REE
165 fractionation patterns.

166 **Methodologies**

167 **Sampling**

168 Samples of the granitic host rocks and the monazite-apatite-Fe(Ti)-oxide mineralization were
169 obtained by channel sampling along two transect through the occurrence using a portable
170 diamond saw. The study focuses on channel samples of: 1) layered monazite-apatite-Fe(Ti)-
171 oxide rocks from the southern (MMKJ037) and northern (MMKJ006) ends of the occurrence,
172 and 2) a fine-grained granoblastic monzonitic aplite dyke (DFKJR006) immediately adjacent to

173 the phosphatic zone at the northern end of the occurrence. Other sample locations shown in
174 Figure 2 are part of a larger regional study by McKeough et al. (2010). The bulk of the
175 analytical work described below was carried out on normal-thickness (~30 μm) polished thin
176 sections.

177 **Electron microscopy**

178 After optical imaging in transmitted and reflected light using a Zeiss AxioImager A1M
179 polarizing microscope, monazite was imaged and analyzed using a JEOL6400 scanning electron
180 microscope (SEM) equipped with an Oxford Prism PGT energy dispersive spectrometer (EDS)
181 and a Gatan Chroma-CL cathodoluminescence system. Backscattered electron (BSE) and
182 cathodoluminescence (CL) images were acquired at 10-15 nA and 15kV with a focused beam.
183 Major element data for monazite was collected on a JEOL733 electron probe microanalyzer
184 (EPMA) equipped with four wavelength dispersive spectrometers (WDS) and Geller dQuant
185 automation software. The analyses were performed at 15kV and 30nA and synthetic REEPO₄
186 glasses used as primary standards for the REE.

187 **LA-ICP-MS**

188 All analyses were carried out using a Resonetics M-50 193nm ArF (excimer) laser ablation
189 system attached to an Agilent 7700x quadrupole ICP-MS with two external rotary pumps and
190 using Iolite™ Trace Elements Data Reduction Scheme (Paton et al., 2011) and VizualAge™ for
191 U-Pb geochronology (Petrus and Kamber, 2012).

192 For trace element mapping, the laser ablation software (Geostar v. 6.23) was used to
193 define a rectangular area within which a number of linear raster scan were defined. Each raster
194 line of the pattern was programmed to run with a crater size of 17 μm , a scan speed of 8 $\mu\text{m}/\text{sec}$,

195 and a laser pulse rate of 10 Hz. The fluence on target was regulated at $4\text{J}/\text{cm}^2$ and the inline
196 smoothing device (the ‘squid’) between the laser and ICP-MS was removed to ensure fastest
197 possible washout from the cell. Ablated aerosol was transported out of the cell using 750 mL/min
198 He and was combined downstream with a 750 mL/min Ar carrier gas flow. A background delay
199 of 20sec was for used for each raster line. Concentration standards (NIST610) and quality
200 control standards (GSE-1G) were ablated before and after the map pattern using the same
201 analytical conditions. A typical trace element map acquisition defined in this way took between
202 30-40 minutes to run. The ICP-MS was tuned using NIST610 in order to maximize sensitivity
203 while also maintaining oxide production (monitored as $^{248}\text{ThO}^+ / ^{232}\text{Th}^+ < 0.3\%$), doubly-charged
204 ions (measured as $^{22}\text{M}^+ / ^{44}\text{Ca}^+$), and $^{238}\text{U}^+ / ^{232}\text{Th}^+ \approx 1.05$. The latter is a measure of plasma
205 robustness. The number of analytes and their dwell times were selected to ensure that the total
206 ICP-MS sweep time was < 0.5 sec. Individual analyte dwell times were assigned to be
207 approximately inversely proportional to the concentration in the target grain. High concentration
208 elements (P, LREE, Th) were set with 0.01 sec dwell times whereas lower concentration
209 elements were set with 0.02 to 0.05 sec dwell times. The total ICP-MS acquisition time was set
210 to correspond to the total time to run through the predefined laser ablation sequence and the two
211 instruments were started simultaneously. At the end of the acquisition, the Geostar laser log file
212 and the Agilent time series data (cps versus time) were combined offline using the Iolite
213 automatic integrations function and the data reduced. The independently (electron microprobe)
214 measured concentration (wt%) of Nd in the monazite target was used as an internal standard.
215 Trace element data for Kulyk Lake monazite was reduced assuming a Nd concentration of
216 9.0wt%. Data for Trebilcock and 44069 monazite were analyzed assuming Nd concentrations of
217 10wt% and 9.8wt% respectively. Quality of the analytical method and data reduction scheme
218 was checked by comparing the measured/accepted values obtained for GSE-1G standard (**Table**

219 1). Absolute values and detection limits for As are anomalously high and are probably related to
220 a wide variety of argide interferences (e.g., $^{36}\text{Ar}^{38}\text{Ar}^1\text{H}^+$, $^{40}\text{Ar}^{35}\text{Cl}^+$, $^{36}\text{Ar}^{39}\text{K}^+$) present in the gas
221 background and produced during ablation. As a result, As concentrations were adjusted
222 downward by ~10% (As* in Tables 3, 4, 5, and 6) to match the upper error limit in GSE-1G (350
223 ppm). The trace element maps presented in Figures 6 and 10 show semi-quantitative
224 concentrations that are calculated without using an internal standard but instead are based on the
225 analyte intensity in the unknown compared to its intensity in NIST610. The semi-quantitative
226 concentrations are typically within 20-30% of the true value and so serve as a reasonable
227 approximation for visualizing different compositional domains.

228 For U-Pb geochronology, the ICP-MS was first tuned using NIST610 to obtain oxide
229 production and U/Th values described above whereas doubly-charged ion production was not
230 strictly monitored. Monazite U-Pb geochronology by LA-ICP-MS was carried out using 14, 17
231 or 26 μm diameter craters depending on the size of the compositional zoning domain targeted for
232 analysis. Ablation was carried out at 4 Hz and 3 J/cm^2 with a 30 sec background and 30 sec
233 ablation. External standardization to correct for laser-induced Pb/U fractionation and mass-bias
234 in the ICP-MS was accomplished by replicate ($n \geq 15$) measurements of either 44069 (425 Ma)
235 or Trebilcock (272 Ma) monazite. The 44069 standard was used primarily for the lowest U
236 concentration domains encountered in the monazite-apatite-ilmenite dyke owing to the better
237 matrix matching compared to the much higher-U Trebilcock standard. Analyses of NIST610 at
238 the start and end of the ablation sequence were additionally used as concentration standards. The
239 ICP-MS was tuned, using a raster scan on NIST610, to achieve maximum sensitivity for ^{207}Pb by
240 adding 2.8 mL/min N_2 to the He + Ar carrier gas and by using the second external rotary pump
241 on the ICP-MS. The analytes and dwell times (in milliseconds) chosen were: ^{31}P (10), ^{146}Nd

242 (10), ^{204}Pb (80), ^{206}Pb (30), ^{207}Pb (80), ^{208}Pb (10), ^{232}Th (10) and ^{238}U (20). No significant ^{204}Pb
243 above the gas blank of ca. 160cps was encountered and so common-Pb corrections are
244 considered to be negligible. The data were processed offline using Iolite™ and VizualAge™.
245 When necessary the data were also corrected for common-Pb using the correction routine
246 described by Andersen (2002) and implemented in VizualAge™ which avoids inaccuracies
247 associated with measuring low concentrations of ^{204}Pb by LA-ICP-MS (Storey et al., 2006).
248 Common-Pb corrected data are highlighted in Table 7. Data quality was confirmed by
249 measuring replicate analyses of one or more in-house standards such as Thompson Mine-2
250 monazite (1765 Ma).

251 **LA-MC-ICP-MS for Sm-Nd**

252 Following optical microscopy and backscattered electron imaging to identify suitable targets, 1
253 cm diameter round target areas were drilled out of a 60 μm thick thin section and mounted in
254 epoxy along with LREE-glass standards described by Fisher et al. (2011) to correct for Sm/Nd
255 fractionation. Measurements were carried out at the Memorial University of Newfoundland
256 CREAiT facility on a GeoLas 193nm laser ablation system connected to a Thermo Neptune MC-
257 ICP-MS. The outermost portions of large monazite grains were analyzed using a 45 μm
258 diameter crater at a repetition rate of 5 Hz and fluence of approximately 5 J/cm^2 . Replicate
259 analyses of LREE-glass ($n = 4$) and Trebilcock monazite ($n = 6$) were used to correct for Sm/Nd
260 bias and to verify that the measured $^{143}\text{Nd}/^{144}\text{Nd}$ and $^{145}\text{Nd}/^{144}\text{Nd}$ values for the standard were
261 within error of the true values. The data were processed offline using an in-house data reduction
262 macro (MCTool-Nd) that was modified from LAMTool-Hf written by J. Kosler, University of
263 Bergen. Corrections for instrumental mass-bias followed the methodology outlined in Fisher et
264 al. (2011). Initial $\epsilon\text{Nd}(t)$ values were calculated on the basis of measured U-Pb ages.

265

Results

266 Petrographic relationships

267 The monazite-apatite-Fe(Ti)-oxide zones display an internal differentiation, with interleaving
268 monazite-rich and apatite-rich bands (Figure 2b). Monazite-rich areas occur as lenses and
269 stringers with a granoblastic interlocking texture and grains sizes between 0.1 to 2 mm. In thin
270 section, boundaries between monazite masses and neighbouring apatite-rich layers are typically
271 sharp, but locally show a gradational transition (Figure 2c). Whereas apatite and monazite form
272 discrete layers, titanomagnetite occurs either as elongate cm-scale clots or as weakly foliated
273 xenomorphic grains interstitial to monazite and apatite (Figure 2c and 3). Grain boundaries
274 between adjacent monazite and apatite are typically straight to curvilinear and well defined
275 triple-junctions exist between the major phases in the rock. Whereas monazite is subhedral to
276 xenomorphic, apatite locally forms euhedral to subhedral hexagonal grains enclosing zircon
277 grains that display core-overgrowth textures (Figure 3a). Radial fractures emanating from zircon
278 inclusions in apatite and titanomagnetite are abundant and this texture is typically associated
279 with volume expansion during metamictization of zircon. Titanomagnetite defines a weak
280 alignment and displays fine (1 to 5 μm wide) exsolution lamellae of ilmenite and rutile. Apatite
281 locally occurs as inclusions in large ilmenite grains whereas monazite inclusions in ilmenite have
282 not been observed. Similarly, apatite inclusions within monazite are rare.

283 Accessory zircon is abundant and is observed primarily along grain boundaries and triple
284 junctions between monazite, apatite and titanomagnetite in addition to being included in every
285 major mineral in the monazite-apatite-Fe(Ti)-oxide zones. Zircon occurs as sub-rounded equant
286 grains up to 75 μm in diameter most of which display a thin 10-20 μm rim that is visible in
287 reflected light, BSE, and CL images (Figure 4).

288 **Major and trace element zoning and chemistry**

289 A combination of BSE and CL imaging were used to examine internal zoning features in
290 monazite, apatite, and titanomagnetite within the mineralized zones. Apatite displays faint
291 patchy zoning in BSE images but no systematic zoning is obvious. Detailed CL imaging of
292 apatite did reveal the presence of numerous darker-CL healed fractures and a cryptic network of
293 dark CL domains that concentrated around zircon grains (Figure 3b). In contrast, backscattered-
294 electron images (Figure 5) of monazite-rich layers reveal at least three compositional domains:
295 1) rare bright-BSE cores surrounded by; 2) darker-BSE oscillatory-zoned domains, and 3)
296 uniform medium-BSE overgrowths that form the interlocking texture noted earlier.

297 The EPMA was used to analyze each of these compositional domains and establish major
298 element monazite compositions that could be used as internal standards for subsequent LA-ICP-
299 MS analyses (Table 2). The LREE (La, Ce, Pr, Nd) abundances uniform and independent of the
300 compositional zoning revealed by BSE imaging. The bulk of the variation in BSE brightness is
301 attributable to the Th content of each domain which varies from 3.3wt% Th in the bright-BSE
302 inner cores to 2.8wt% in dark-BSE areas of oscillatory-zoned domains to 4.3% in the uniform
303 overgrowths. Uranium concentrations measured by electron microprobe were typically below
304 detection limit (<0.02wt%) under the analytical conditions employed for EPMA major-element
305 analyses.

306 Three LA-ICP-MS maps were constructed to help guide the location of *in-situ* U-Pb
307 geochronology measurements. These maps (Figure 6) not only revealed the presence of low-U
308 cores that correspond to the dark-BSE domains in Figure 5, they also show that within these core
309 domains exist partially-resorbed monazite characterized by anomalously high V, As, and Mo as

310 well as distinct $(La/Yb)_{CN}$ and Th/U. Based on the LA-ICP-MS maps it is, therefore, possible to
311 further sub-divide the cores into several sub-domains based on their trace element composition.

312 Once the LA-ICP-MS mapping session was complete, the thin sections were removed
313 from the laser ablation cell and re-polished using 3 μ m diamond paste to remove the bulk of the
314 surface damage induced by the laser raster pattern used to generate the trace element maps. The
315 samples were reloaded into the cell and images showing either the As or V concentration were
316 overlain on the reflected light image of the target grain captured by the laser ablation software.
317 This allowed specific compositional domains revealed in the LA-ICP-MS maps to be targeted for
318 trace element spot analyses using 13 μ m craters. Figure 7 shows how an overlay showing the
319 distribution of V in monazite grain 2 was used to carefully position the location of craters used to
320 characterize the compositional variability of monazite and corresponding U-Pb ages.

321 The results of the LA-ICP-MS spot analyses are shown in Tables 3, 4, and 5. For
322 comparison, two widely-used monazite standards, Trebilcock monazite (Tomascak et al., 1998)
323 and 44069 (Aleinikoff et al., 2006) were also analyzed for comparison and the results are given
324 in Table 6. Data for the Chondrite-normalized (McDonough and Sun, 1995) REE show only
325 minor variations among the different compositional domains identified. Taken as a group,
326 monazite from the phosphate-Fe(Ti)-oxide zones displays strongly-fractionated REE patterns
327 (Figure 8) with $(La/Yb)_{CN}$ ranging from 1000 to 1400 compared to \sim 125 and \sim 200 for Trebilcock
328 and 44069 respectively. Kulyk Lake monazite also contains \sim 1000 ppm Eu and displays a small
329 (0.25) negative Eu/Eu* anomaly. The LA-ICP-MS data also confirm the low concentrations of
330 both U (75-350 ppm) and Th (2.2 to 5.5 wt%). The domains containing elevated V, As, and Mo
331 display concentrations in the 100-350 ppm range for V, 1200-1750 ppm for As, and 4 to 9 ppm
332 Mo. These domains also contain low and variable amounts of Ba and Nb. For comparison, the

333 pegmatite-hosted Trebilcock monazite does not contain V, Mo, Nb, and Ba above detection
334 limits (1.4, 0.34, 0.18 and 0.21 ppm respectively) and has ~589 ppm As. The 44069 standard
335 does contain measureable V (2.8 ppm) and has a somewhat lower As content of ~470 ppm.

336 **U-Pb geochronology**

337 Results of *in-situ* U-Pb dating of different compositional domains in monazite revealed by BSE
338 imaging and mapped by LA-ICP-MS in grains 1, 2, and 3 as well as data for the host aplitic
339 monzonite are presented in Table 7. The partially resorbed domains characterized by elevated
340 As, V, and Mo define an array of near-concordant data with $^{207}\text{Pb}/^{206}\text{Pb}$ ages ranging from ~1870
341 to ~2000 Ma with significant populations at ~1880 Ma and 1975 Ma (Figure 9 probability
342 density).

343 The measured $^{207}\text{Pb}/^{206}\text{Pb}$ ages are strongly correlated with compositional zoning in the
344 monazite grains for which LA-ICP-MS trace element maps were constructed. Figure 10 shows
345 the V, Th/U and Mo semi-quantitative compositional maps for monazite grain 3 as well as the
346 $^{207}\text{Pb}/^{206}\text{Pb}$ age. Domains with elevated Mo up to 10 ppm and intermediate Th/U gave somewhat
347 near-concordant common-Pb corrected data with $^{207}\text{Pb}/^{206}\text{Pb}$ dates in the range of 1876 to 1920
348 Ma. The compositional domain characterized by the lowest Th/U value display a similarly
349 narrow range of near-concordant data with $^{207}\text{Pb}/^{206}\text{Pb}$ dates between 1870 to 1897 Ma. This
350 grain contains a distinct core characterized by low V, Mo and U as well as distinctly higher Th/U
351 compared the other compositional domains. Two craters on this domain produced discordant U-
352 Pb data with common-Pb corrected $^{207}\text{Pb}/^{206}\text{Pb}$ dates of ~1850 Ma suggesting it may represent an
353 embayment of younger overgrowth material.

354 The results for the uniform-BSE overgrowths (Figure 11a and 11b) also display a
355 spectrum of near-concordant ages ranging from ~1770 to ~1850 Ma with two populations of
356 overlapping data at 1768 ± 10 Ma ($n = 5$) and 1838 ± 10 Ma ($n = 7$).

357 The host monzonitic aplite dyke to the monazite-apatite-Fe(Ti)-oxide occurrence also
358 contains abundant and large monazite grains with similar core-overgrowth relationships as
359 imaged by BSE. In order to constrain the crystallization age of the aplite dyke, uniform-BSE
360 overgrowths were specifically targeted to avoid mixing between older inherited components.
361 The results of this dating, shown in Figure 11c and 11d are identical within error to those
362 obtained for the monazite within the mineralized zone: a cluster of overlapping dates at 1787 ± 8
363 Ma ($n = 4$) and another at 1827 ± 8 Ma ($n = 4$).

364 Zircon cores and overgrowths were also dated by LA-ICP-MS to help identify their
365 origin. The results of zircon dating, compiled in Table 8, reveal a similarly wide spectrum of
366 $^{207}\text{Pb}/^{206}\text{Pb}$ ages ranging from ~1800 to 2350 Ma with populations at 1895 Ma and 1975 Ma.
367 Higher reflectance zircon overgrowths shown in Figure 4 are not obviously younger. Rather,
368 these overgrowths and the cores they surround are both locally reset to ~1800 Ma.

369 **Sm-Nd isotope systematics**

370 The uniform overgrowths on Kulyk Lake monazite have uniform $^{143}\text{Nd}/^{144}\text{Nd}$ as measured by
371 LA-MC-ICP-MS with $\epsilon\text{Nd}(t)$ values calculated at 1830 ± 10 Ma between -5.0 and -5.7 (Table 9).
372 There is very little intergranular variation in $^{147}\text{Sm}/^{144}\text{Nd}$ and depleted mantle model ages (T_{DM})
373 average 2400 Ma.

374 **Discussion**

375 **Timing of and temperature of emplacement**

376 Both the monazite-apatite-Fe(Ti)-oxide occurrence and the adjacent aplitic dyke contain
377 monazite overgrowths with statistically indistinguishable U-Pb monazite ages. In both rocks, the
378 age of crystallization of compositionally uniform overgrowths is 1830 ± 5 Ma. This date falls in
379 the range of estimates for the timing of granulite-facies metamorphism in the region related to
380 Trans-Hudson crustal thickening and orogenesis (Annesley et al., 2005). This timing of
381 crystallization is consistent with the oxygen-isotope temperature estimates of $>850^\circ\text{C}$ described
382 by McKeough (2013) for monazite-apatite and monazite-titanomagnetite fractionation. This
383 high temperature estimate is also consistent with the presence of exsolved ilmenite and rutile in
384 the Fe(Ti)-oxide phase. The discordant nature of the host granitic dykes with respect to the
385 regional gneissic fabric shown in Figure 2 would reflect emplacement of anatectic melts derived
386 from deeper levels into syn-kinematic dilatational jogs developed at higher structural levels (e.g.,
387 Marchildon and Brown, 2003; Solar et al., 1998). The younger 1770 ± 10 Ma population in both
388 rocks matches the timing of pegmatite emplacement associated with the late stages of isothermal
389 decompression and transpressive deformation at amphibolite-facies conditions (Annesley et al.,
390 2005; Hou et al., 2012). The localized resetting of U-Pb ages measured in monazite and zircon is
391 most likely associated with this post-peak metamorphic reworking. Evidence for the localized
392 nature of this overprint may be recorded by the cryptic dark-CL network in apatite that suggests
393 these zones were locally recrystallized in the vicinity of zircon and along fractures that were
394 subsequent healed. Hence, it appears that whereas the monazite overgrowths in the monazite-
395 apatite-Fe(Ti)-oxide zones and the adjacent aplitic monzonite co-crystallized at 1830 ± 5 Ma, the
396 entire sequence was later affected by dynamic recrystallization and localized Pb-loss along a
397 cryptic fracture-controlled network.

398 **Significance of As, V, Mo in inherited cores**

399 A large volume fraction of the monazite in the phosphate-Fe(Ti)-oxide zone is inherited from the
400 Wollaston Group metasediments. The *in-situ* Sm-Nd isotope systematics measured on 1830 ± 5
401 monazite domains have $\epsilon\text{Nd}_{(1830)}$ ranging from -4.3 ± 0.8 to -5.0 ± 0.8 and these fall within the
402 range of wholerock $\epsilon\text{Nd}_{(1830)}$ values (-4.1 to -7.6) documented by Tran et al. (2010) for the
403 Wollaston Domain. This confirms their derivation from reworked Wollaston Group
404 metasedimentary rocks and implicates high-temperature anatexis as a source of the granitic
405 melts. It is not possible to identify exactly which part (i.e., upper or lower succession) of the
406 volcano-sedimentary succession the rocks were derived from, although the dominantly
407 Paleoproterozoic detrital monazite and zircon population and less evolved $\epsilon\text{Nd}_{(1830)}$ signature are
408 broadly consistent with an upper Wollaston Group source. Based solely on the areal-percentages
409 of oscillatory zoned and dark-BSE cores in Figure 5, 15 - 20% by volume of the monazite is
410 inherited. An even larger volume fraction of zircon is detrital in origin based on the proportion
411 of narrow overgrowths to resorbed cores. The provenance of these components broadly matches
412 the detrital zircon populations measured elsewhere in the middle succession of the Wollaston
413 domain (Su et al., 2012).

414 The xenocrystic components in monazite (i.e., >1880 Ma) have trace element
415 compositions that are anomalously enriched in As, V, and locally Mo, Nb, and Ba compared to
416 monazite found in peraluminous granitic pegmatites (Trebilcock) and associated with
417 amphibolite-facies psammitic and pelitic metasedimentary gneisses (44069). The Kulyk Lake
418 monazite also displays strongly-fractionated REE patterns with $(\text{La}/\text{Yb})_{\text{CN}} > 1000$ compared to
419 values of <200 for Trebilcock and 44069. Additional compositional anomalies in the inherited
420 cores such as a small negative Eu-anomaly (0.25) and Th/U between 250 and 550 also contrast
421 with monazite in the limited number studies in which it was analyzed by LA-ICP-MS in

422 metamorphic and magmatic systems (Bea and Montero, 1997; Bea et al., 1994; Gregory et al.,
423 2009; Hermann and Rubatto, 2003; McFarlane and Frost, 2008; Rubatto et al., 2001) . These
424 observations are most compatible with a portion of the inherited monazite being derived from
425 metalliferous black shales that share similar enrichment in Mo, V, As, and Ba (e.g., Breit et al.,
426 1989; Desborough et al., 1989) as well elevated LREE/HREE (Lehmann et al., 2007). The
427 formation of authigenic monazite nodules in a variety of Ca-poor sedimentary lithologies
428 (Borisova et al., 2010; Bouch et al., 2002) and especially REE-enriched metalliferous black
429 shales (Alipour-Asll et al., 2012) provides a viable mechanism for the formation of abundant As,
430 V, Mo, and LREE-enriched monazite prior to partial melting associated with peak-
431 metamorphism during the Trans-Hudson orogeny.

432 The existence of abundant xenocrystic monazite and zircon components, mineralogical
433 similarities with the neighbouring monzonite dyke, timing with respect to peak Trans-Hudson
434 metamorphism, and high-temperature crystallization inferred from oxygen-isotope data
435 (McKeough, 2013) preclude hydrothermal vein deposition processes for the monazite-apatite-
436 Fe(Ti)-oxide occurrence. The abundance of inherited monazite and zircon in the monazite-
437 apatite-Fe(Ti)-oxide zone leaves little doubt that entrainment of either detrital or diagenetic
438 phosphates was an important process in the source region to these rocks. Entrainment of
439 xenocrystic monazite and zircon have been identified elsewhere in pegmatite-related U-Th-REE
440 occurrences in the region such as Frasers Lake (McKechie et al., 2013) and Yellow (Karin)
441 Lake (McKeough et al., 2010). In these occurrences monazite, apatite, zircon, Fe(Ti)-oxide and
442 biotite typically occur as glomerophorphic masses, locally forming cm-scale lenses. Although
443 a detrital origin for some part of the apatite in the phosphatic zone at Kulyk Lake could not be
444 confirmed, detrital and diagenetic apatite are both common constituents in marine sediments

445 (Bouch et al., 2002; Morton and Yaxley, 2007). Reconnaissance LA-ICP-MS trace element
446 mapping of apatite failed to reveal core-overgrowth relationships similar to those preserved by
447 monazite and zircon and the locally euhedral habit of apatite (e.g., Figure 3a) and the more
448 widespread occurrence of zircon inclusions in apatite compared to monazite suggests that the
449 bulk of the apatite may have crystallized from the anatectic melt.

450 Partial melting of source rocks already enriched in either detrital or diagenetic phosphates
451 is, therefore, a potentially viable mechanism to account for the observed volume fraction of
452 inherited material in the monazite-apatite-Fe(Ti)-oxide zone. Given the limited solubility of
453 monazite and apatite in low- $a_{\text{H}_2\text{O}}$ metaluminous (ASI ~ 1) to weakly peraluminous (ASI < 1.3)
454 granitic liquids derived from biotite-dehydration melting at granulite-facies conditions (Montel,
455 1993; Rapp and Watson, 1986; Watson et al., 1989; Wolf and London, 1994; Wolf and London,
456 1995) the preservation of inherited xenocrystic phosphate components is likely. Entrainment of
457 xenocrystic components was apparently followed by magmatic (cotectic) crystallization of
458 monazite, zircon, and apatite followed by emplacement coevally with the granitic dykes. The
459 observed textural relationships between monazite, apatite, zircon, and titanomagnetite suggest
460 that cotectic crystallization of overgrowths on monazite and zircon occurred prior to
461 titanomagnetite crystallization, the latter typically occurring interstitial to monazite but locally
462 occluding apatite and zircon. Apatite grain morphology varies from euhedral to anhedral,
463 suggesting that it may have crystallized over a wider range of conditions. The interstitial and
464 locally oikocrystic nature of titanomagnetite in the phosphatic zones (see Figure 2c) is
465 reminiscent of an intercumulus texture.

466 **Revealing source controls on pegmatite fertility**

467 The in-situ LA-(MC)-ICP-MS techniques applied here have revealed compelling evidence for
468 the involvement of potentially metalliferous protoliths in the anatectic source region to the
469 pegmatite bodies at Kulyk Lake. This evidence is preserved primarily as complex intragranular
470 zoning in monazite of elements such as V, As, Mo, Nb, Ba, Eu, (La/Yb)_{CN}, and Th/U. Many of
471 these elements occur at concentrations (<10 ppm) well below practical operating conditions for
472 EPMA and so LA-(MC)-ICP-MS trace element mapping is a critical first step in assessing
473 evidence for inheritance in these S-type magmatic systems. Linking high-precision U-Pb isotope
474 geochronology with compositional zoning for these low-abundance trace elements is also critical
475 for resolving inherited xenocrystic components from those that crystallized from the
476 differentiated granitic liquid.

477 The trace element composition of 1830 Ma magmatic overgrowths analyzed by LA-ICP-
478 MS spot analyses may also reveal details of magmatic differentiation and fractionation processes
479 in contaminated peraluminous magmas. For example, discontinuous 1830 Ma overgrowths have
480 higher absolute concentrations of U and Mo compared to the xenocrystic domains. This
481 enrichment of incompatible U and Mo is typically associated with fractional crystallization of
482 granitic magmas (e.g., Blevin and Chappell, 1995). The concentrations of V, As, Nb, Mo, and
483 Ba encountered in the magmatic overgrowths at Kulyk Lake are also higher than those measured
484 for either the monazite from the Trebilcock pegmatite (Tomascak et al., 1998) or from regional
485 metamorphic monazite (44069) from the Wilmington Complex, Delaware (Aleinikoff et al.,
486 2006). Hence, monazite that crystallized from variably fractionated granitic liquid at the Kulyk
487 Lake monazite-apatite-Fe(Ti)-oxide occurrence appears to faithfully record anomalous
488 geochemical signatures related to source-rock entrainment and partial assimilation processes
489 (McKeough, 2013). Source rock heterogeneity of this nature has been identified in other granitic

490 systems on the basis of textural, major-element, and isotopic heterogeneity (Clemens et al.,
491 2010). Monazite zoning patterns and concentration anomalies for the broad range of trace
492 elements measurable using LA-ICP-MS could provide another method of exploring source
493 heterogeneity in peraluminous granitic melts.

494 **Implications**

495 This study illustrates how the integration of *in-situ* LA-(MC)-ICP-MS trace element mapping, U-
496 Pb geochronology, trace-element spot analyses, and *in-situ* Nd-isotope systematics on monazite
497 may be combined to reveal details of REE-phosphate occurrences associated with granitoid
498 intrusions. In particular, the integration of LA-ICP-MS trace element mapping and high-spatial
499 resolution compositionally-guided U-Pb geochronology may be used to distinguish between
500 xenocrystic and magmatic components in these systems that may otherwise be missed using
501 conventional approaches. The results obtained here for the monazite-apatite-Fe(Ti)-oxide
502 occurrence also suggests that the prospectivity of REE-enriched pegmatite corridors in the
503 Wollaston Domain and, by extension, other high-grade metasedimentary belts, could be identified
504 using monazite geochemistry as a tracer of fertile metalliferous source rocks at depth. Applying
505 similar techniques to other unusual phosphatic deposits may help identify processes related
506 source lithology, xenocryst entrainment, assimilation, and fractional crystallization that are
507 preserved as relict trace element and Nd-isotope zoning features now easily revealed by LA-
508 (MC)-ICP-MS.

509 **Acknowledgements**

510 The authors are grateful to Dr. D. Hall and S. Cogswell (UNB Microscopy and Microanalysis
511 Facility) and Dr. Y. Luo (UNB LA-ICP-MS facility) for their patient help with the analyses. We

512 would also like to acknowledge Dr. C. Fisher, Dr. R. Lam (Memorial University of
513 Newfoundland, CREAT) and C. Laflamme for acquiring and reducing LA-MC-ICP-MS data for
514 Sm-Nd in monazite. This research was supported by an NSERC Discovery Grant to C.R.M.M.
515 and by financial and in-kind support from the Saskatchewan Geological Survey and Eagle Plains
516 Resources Ltd. The manuscript benefited from constructive reviews by K. Ansdell, G. Morgan,
517 and C. Allen.

518 **References**

- 519 Alagna, K.E., Petrelli, M., Perugini, D., and Poli, G. (2008) Micro-analytical zircon and
520 monazite U-Pb isotope dating by laser ablation-inductively coupled plasma-quadrupole
521 mass spectrometry. *Geostandards and Geoanalytical Research*, 32, 103-120.
- 522 Aleinikoff, J.N., Schenck, W.S., Plank, M.O., Srogi, L., Fanning, C.M., Kamo, S.L., and
523 Bosbyshell, H. (2006) Deciphering igneous and metamorphic events in high-grade rocks
524 of the Wilmington Complex, Delaware: Morphology, cathodoluminescence and
525 backscattered electron zoning, and SHRIMP U-Pb geochronology of zircon and
526 monazite. *Geological Society of America bulletin*, 118, 39-64.
- 527 Alipour-Asll, M., Mirnejad, H., and Milodowski, A.E. (2012) Occurrence and paragenesis of
528 diagenetic monazite in the upper Triassic black shales of the Marvast region, South Yazd,
529 Iran. *Mineralogy and Petrology*, 104(3-4), 197-210.
- 530 Andersen, T. (2002) Correction of common lead in U-Pb analyses that do not report ^{204}Pb .
531 *Chemical Geology*, 192, 59-79.
- 532 Annesley, I.R., Madore, C., and Krogh, T.E. (1992) U-Pb zircon, titanite, and monazite ages
533 from the Wollaston Domain: A summary. . Summary of investigations, Saskatchewan
534 Geological Survey, Report 92-4, 61-65.

- 535 Annesley, I.R., Madore, C., and Portella, P. (2005) Geology and thermotectonic evolution of the
536 western margin of the Trans-Hudson Orogen: evidence from the eastern sub-Athabasca
537 basement, Saskatchewan. *Canadian Journal of Earth Sciences*, 42, 573-597.
- 538 Ayers, J.C., Loflin, M., Miller, C.F., Barton, M.D., and Coath, C.D. (2006) Monazite used to
539 determine the extent and timing of fluid infiltration in the Birch Creek Pluton
540 metamorphic aureole. *Geology*, 34, 653-656.
- 541 Bea, F., and Montero, P.G. (1997) Rare earth elements, yttrium, thorium, and uranium in crustal
542 melting; the behavior of accessories during metamorphism and anatexis of metapelites;
543 the Kinzigite Formation (Ivrea-Verbano, northern Italy). Seventh annual V M
544 Goldschmidt conference, 921;, p. 21. Lunar and Planetary Institute, Houston, TX, United
545 States.
- 546 Bea, F., Pereira, M.D., and Stroh, A. (1994) Mineral/leucosome trace-element partitioning in a
547 peraluminous migmatite (a laser-ablation-ICP-MS study). *Chemical Geology*, 117, 291-
548 312.
- 549 Bickford, M., Collerson, K., Lewry, J., Van Schmus, W.R., and Chiarenzelli, J. (1990)
550 Proterozoic collisional tectonism in the Trans-Hudson orogen, Saskatchewan. *Geology*,
551 18, 14-18.
- 552 Bickford, M., Mock, T., Steinhart III, W., Collerson, K., and Lewry, J. (2005) Origin of the
553 Archean Sask Craton and its extent within the Trans-Hudson Orogen: evidence from Pb
554 and Nd isotopic compositions of basement rocks and post-orogenic intrusions. *Canadian
555 Journal of Earth Sciences*, 42, 659-684.
- 556 Blevin, P.L., and Chappell, B.W. (1995) Chemistry, origin and evolution of mineralised
557 granitoids in the Lachlan Fold Belt, Australia: the metallogeny of I- and S-type
558 granitoids. *Economic Geology*, 90, 1604-1619.

- 559 Borisova, A.Y., Freydier, R., Polve, M., Jochum, K.P., and Candaudap, F. (2010) Multi-
560 Elemental Analysis of ATHO-G Rhyolitic Glass (MPI-DING Reference Material) by
561 Femtosecond and Nanosecond LA-ICP-MS: Evidence for Significant Heterogeneity of B,
562 V, Zn, Mo, Sn, Sb, Cs, W, Pt and Pb at the Millimetre Scale. *Geostandards and*
563 *Geoanalytical Research*, 34(3), 245-255.
- 564 Bosch, D., Hammor, D., Bruguier, O., Caby, R., and Luck, J.-M. (2002) Monazite "in situ"
565 ²⁰⁷Pb/²⁰⁶Pb geochronology using a small geometry high-resolution ion probe.
566 Application to Archaean and Proterozoic rocks. *Chemical Geology*, 184, 151-165.
- 567 Bouch, J.E., Hole, M.J., Trewin, N.H., Chenery, S., and Morton, A.C. (2002) Authigenic apatite
568 in a fluvial sandstone sequence: evidence for rare-earth element mobility during
569 diagenesis and a tool for diagenetic correlation. *Journal of Sedimentary Research*, 72(1),
570 59-67.
- 571 Breecker, D.O., and Sharp, Z.D. (2007) A monazite oxygen isotope thermometer. *American*
572 *Mineralogist*, 92, 1561-1572.
- 573 Breit, G.N., Wanty, R.B., and Tuttle, M.L. (1989) Geochemical control on the abundance of
574 vanadium in black shales and related rocks. In R.I. Grauch, and H.L.O. Huyck, Eds.
575 *Metalliferous Black Shales and Related Ore Deposits - Proceedings, 1989 United States*
576 *Working Group Meeting, International Geological Correlation Program Project 254*, p. 6-
577 11. U.S. Geological Survey Circular 1058.
- 578 Cherniak, D.J., Watson, B.E., Grove, M., and Harrison, T.M. (2004) Pb diffusion in monazite: a
579 combined RBS/SIMS study. *Geochimica et Cosmochimica Acta*, 68, 829-840.
- 580 Chiarenzelli, J. (1989) Petrogenesis and tectonic significance of the Guncoat and Nistowiak
581 gneisses, Glennie Lake Domain, northern Saskatchewan, Ph.D., p. 229. University of
582 Kansas.

- 583 Chiarenzelli, J., Aspler, L., Lewry, J., and Villeneuve, M. (1998) Early Proterozoic evolution of
584 the Saskatchewan Craton and its allochthonous cover, Trans-Hudson Orogen. *Journal of*
585 *Geology*, 106, 247-267.
- 586 Clemens, J.D., Helps, P.A., and Stevens, G. (2010) Chemical structure in granitic magmas - a
587 signal from the source? *Earth and Environmental Science Transactions of the Royal*
588 *Society of Edinburgh*, 100, 159-172.
- 589 Desborough, G.A., Hatch, J.R., and Leventhal, J.S. (1989) Geochemical and mineralogical
590 comparison of the upper Pennsylvanian Stark Shale Member of the Dennis Limestone,
591 east-central Kansas, with the Middle Pennsylvanian Mecca Quarry Shale Member of the
592 Carbondale Formation in Illinois and the Linton Formation in Indiana. In R.I. Grauch,
593 and H.L.O. Huyck, Eds. *Metalliferous Black Shales and Related Ore Deposits -*
594 *Proceedings, 1989 United States Working Group Meeting, International Geological*
595 *Correlation Program Project 254*, p. 12-30. U.S. Geological Survey Circular 1058.
- 596 Fisher, C.M., McFarlane, C.R.M., Hanchar, J.M., Schmitz, M.D., Sylvester, P.J., Lam, R., and
597 Longerich, H.P. (2011) Sm-Nd Isotope Systematics by Laser-Ablation-Multicollector-
598 Inductively Coupled Plasma Mass Spectrometry: Methods and Potential Natural and
599 Synthetic Reference Materials. *Chemical Geology*, 284, 1-20.
- 600 Fitzsimons, I.C.W., Kinny, P.D., and Harley, S.L. (1997) Two stages of zircon and monazite
601 growth in anatectic leucogneiss: SHRIMP constraints on the duration and intensity of
602 Pan-African metamorphism in Prydz Bay, East Antarctica. *Terra Nova*, 9, 47-51.
- 603 Forbes, C.J., Giles, D., Betts, P.G., Weinberg, R., and Kinny, P.D. (2007) Dating prograde
604 amphibolite and granulite facies metamorphism using in situ monazite U-Pb SHRIMP
605 analysis. *Journal of Geology*, 115, 691-705.

- 606 Gregory, C.J., McFarlane, C.R.M., Hermann, J., and Rubatto, D. (2009) Tracing the evolution of
607 calc-alkaline magmas: In-situ Sm-Nd isotope studies of accessory minerals in the Bergell
608 Igneous Complex, Italy. *Chemical Geology*, 260, 73-86.
- 609 Hermann, J., and Rubatto, D. (2003) Relating zircon and monazite domains to garnet growth
610 zones; age and duration of granulite facies metamorphism in the Val Malenco lower
611 crust. *Journal of Metamorphic Geology*, 21(9), 833-852.
- 612 Hoffman, P.F. (1989) Precambrian geology and tectonic history of North America. In A.W.
613 Bally, and A.R. Palmer, Eds. *The Geology of North America*, A, p. 447-512. Geological
614 Society of America.
- 615 -. (1990) Subdivision of the Churchill province and extent of the Trans-Hudson Orogen. In J.F.
616 Lewry, and M.R. Stauffer, Eds. *The Early Proterozoic Trans-Hudson Orogen of North*
617 *America*, Special Paper 37, p. 15-39. Geological Association of Canada.
- 618 Hou, T., Zhang, Z.C., and Pirajno, F. (2012) A new metallogenic model of the Panzihua giant
619 V-Ti-iron oxide deposit (Emeishan Large Igneous Province) based on high-Mg olivine-
620 bearing wehrlite and new field evidence. *International Geology Review*, 54(15), 1721-
621 1745.
- 622 Hu, M.Y., Fan, X.T., Stoll, B., Kuzmin, D., Liu, Y., Liu, Y.S., Sun, W.D., Wang, G., Zhan, X.C.,
623 and Jochum, K.P. (2011) Preliminary Characterisation of New Reference Materials for
624 Microanalysis: Chinese Geological Standard Glasses CGSG-1, CGSG-2, CGSG-4 and
625 CGSG-5. *Geostandards and Geoanalytical Research*, 35(2), 235-251.
- 626 Kelsey, D.E., Clark, C., and Hand, M. (2008) Thermobarometric modelling of zircon and
627 monazite growth in melt-bearing systems: examples using model metapelitic and
628 metapsammitic granulites. *Journal of Metamorphic Geology*, 26, 199-212.

- 629 Lehmann, B., Nagler, T.F., Holland, H.D., Wille, M., Mao, J., Pan, J., Ma, D., and Dulski, P.
630 (2007) Highly metalliferous carbonaceous shale and Early Cambrian seawater. *Geology*,
631 35, 403-406.
- 632 Lewry, J.F., and Collerson, K.D. (1990) The Trans-Hudson Orogen: Extent, subdivision and
633 problems. In J.F. Lewry, and M.R. Stauffer, Eds. *The Early Proterozoic Trans-Hudson*
634 *Orogen of North America*, Special Paper 37, p. 1-14. Geological Association of Canada.
- 635 Lewry, J.F., and Sibbald, T.I.I. (1980) Thermotectonic evolution of the Churchill Province in
636 northern Saskatchewan. *Tectonophysics*, 68, 45-82.
- 637 Marchildon, N., and Brown, M. (2003) Spatial distribution of melt-bearing structures in anatectic
638 rocks from southern Brittany, France: implications for melt transfer at grain- to orogen-
639 scale. *Tectonophysics*, 364, 215-235.
- 640 Mawdsley, J.B. (1957) *The Geology of the Middle Foster Lake Area, Northern Saskatchewan*.
641 Saskatchewan Geological Survey, Report 26, 45.
- 642 McDonough, W.F., and Sun, S.-S. (1995) Composition of the Earth. *Chemical Geology*, 120,
643 223-253.
- 644 McFarlane, C.R.M., and Frost, B.R. (2008) Constraints on the early metamorphic evolution of
645 Broken Hill, Australia, from in-situ U-Pb dating and REE geochemistry of monazite.
646 *Journal of Metamorphic Geology*, in press.
- 647 McFarlane, C.R.M., and Harrison, T.M. (2006) Pb-diffusion in monazite: constraints from a
648 high-T contact aureole setting. *Earth and Planetary Science Letters*, 250, 376-384.
- 649 McKechnie, C.L., Annesley, I.R., and Andsdell, K.M. (2013) Geological Setting, Petrology, and
650 Geochemistry of Granitic Pegmatites and Leucogranites Hosting U-Th-REE
651 Mineralization at Fraser Lakes Zone B, Wollaston Domain, Northern Saskatchewan,
652 Canada. *Exploration and Mining Geology*, 21, 1-26.

- 653 McKeough, M.A. (2013) The Geochemical, Geochronologic, and Isotopic Constraints on U-Th-
654 REE Pegmatites of the Wollaston Domain, Northern Saskatchewan, Canada. Department
655 of Earth Sciences, MSc. University of New Brunswick, Fredericton NB.
- 656 McKeough, M.A., and Lentz, D. (2011) Paleoproterozoic late-tectonic granitic pegmatite-hosted
657 U-Th±REE-Y-Nb mineralization, northern Saskatchewan: products of assimilation,
658 fractional crystallization, and hybridization processes. Summary of Investigations 1997,
659 Saskatchewan Geological Survey, Miscellaneous Report 2011-4.2, paper A-6, 21p.
- 660 McKeough, M.A., Lentz, D.R., and Brown, J.A. (2010) Geology and associated pegmatite- and
661 vein-hosted uranium mineralization of the Kulyk, Eagle, and Karin Lakes regions,
662 Wollaston Domain, northern Saskatchewan. Summary of investigations, Saskatchewan
663 Geological Survey Miscellaneous Report 2010-4.2, Paper A-6, 23.
- 664 Montel, J.M. (1993) A model for monazite/melt equilibrium and application to the generation of
665 granitic magmas. *Chemical Geology*, 110, 127-146.
- 666 Morton, A.C., and Yaxley, G. (2007) Detrital apatite geochemistry and its application in
667 provenance studies. *Geological Society of American Special Paper*, 420, 319-344.
- 668 Paton, C., Hellstrom, J.C., Paul, B., Woodhead, J.D., and Hergt, J.M. (2011) Iolite: Freeware for
669 the visualisation and processing of mass spectrometric data. *Journal of Analytical Atomic*
670 *Spectrometry*, 26, 2508-2518.
- 671 Petrus, J.A., and Kamber, B.S. (2012) VizualAge: A novel approach to laser ablation ICP-MS U-
672 Pb geochronology data reduction. *Geostandards and Geoanalytical Research*, 36, 247-
673 270.
- 674 Rapp, R.P., and Watson, E.B. (1986) Monazite solubility and dissolution kinetics: implications
675 for the thorium and light rare earth chemistry of felsic magmas. *Contributions to*
676 *Mineralogy and Petrology*, 94, 304-316.

- 677 Ray, G.R., and Wanless, R.K. (1980) The age and geological history of the Wollaston, Peter
678 Lake, and Rottenstone domains in northern Saskatchewan. *Canadian Journal of Earth
679 Sciences*, 17, 333-347.
- 680 Rayner, N.M., Stern, R.A., and Bickford, M.E. (2005) Tectonic implications of new SHRIMP
681 and TIMS U–Pb geochronology of rocks from the Sask craton, Peter Lake Domain, and
682 Hearne margin, Trans-Hudson Orogen, Saskatchewan. *Canadian Journal of Earth
683 Sciences*, 42, 635-657.
- 684 Regnery, J., Stoll, B., and Jochum, K.P. (2010) High-Resolution LA-ICP-MS for Accurate
685 Determination of Low Abundances of K, Sc and Other Trace Elements in Geological
686 Samples. *Geostandards and Geoanalytical Research*, 34(1), 19-38.
- 687 Rubatto, D., Williams, I.S., and Buick, I.S. (2001) Zircon and monazite response to prograde
688 metamorphism in the Reynolds Range, central Australia. *Contributions to Mineralogy &
689 Petrology*, 140, 458-468.
- 690 Seydoux-Guillame, A.M., Paquette, J.L., Wiedenbeck, M., Montel, J.M., and Heinrich, W.
691 (2002) Experimental resetting of the U-Th-Pb systems in monazite. *Chemical Geology*,
692 191, 165-181.
- 693 Solar, G.S., Pressley, R.A., Brown, M., and Tucker, R.D. (1998) Granite ascent in convergent
694 orogenic belts; testing a model. *Geology (Boulder)*, 26(8), 711-714.
- 695 Storey, C.D., Jeffries, T.E., and Smith, M. (2006) Common lead-corrected laser ablation ICP-MS
696 U-Pb systematics and geochronology of titanite. *Chemical Geology*, 227, 37-52.
- 697 Su, B.X., Zhang, H.F., Yang, Y.H., Sakyi, P.A., Ying, J.F., and Tang, Y.J. (2012) Breakdown of
698 orthopyroxene contributing to melt pockets in mantle peridotite xenoliths from the
699 Western Qinling, central China: constraints from in situ LA-ICP-MS mineral analyses.
700 *Mineralogy and Petrology*, 104(3-4), 225-247.

- 701 Tomascak, P.B., Krogstad, E.J., and Walker, R.J. (1998) Sm-Nd isotope systematics and the
702 derivation of granitic pegmatites in southwestern Maine, USA. *Canadian Mineralogist*,
703 36, 327-337.
- 704 Tran, H.T., Ansdell, K., Bethune, K., Watters, B., and Ashton, K. (2003) Nd isotope and
705 geochemical constraints on the depositional setting of Paleoproterozoic metasedimentary
706 rocks along the margin of the Archean Hearne craton, Saskatchewan, Canada.
707 *Precambrian Research*, 123, 1-28.
- 708 Tran, H.T., Ansdell, K., Bethune, K.M., ashton, K., and Hamilton, M.A. (2008) Provenance and
709 tectonic setting of Paleoproterozoic metasedimentary rocks along the eastern margin of
710 the Hearne craton: constraints from SHRIMP geochronology, Wollaston Group,
711 Saskatchewan, Canada. *Precambrian Research*, 167, 171-185.
- 712 Tran, H.T., and Yeo, G.M. (1997) Geology of the Burbidge Lake–Northern Upper Foster Lake
713 area, eastern Wollaston Domain (NTS 74A-14). Summary of Investigations 1997,
714 Saskatchewan Geological Survey, Miscellaneous Report 97-4, 72-89.
- 715 Watkinson, D.H., and Mainwaring, P.R. (1976) The Kulyk Lake monazite deposit, northern
716 Saskatchewan. *Canadian Journal of Earth Sciences*, 13, 470-475.
- 717 Watson, E.B., Vicenzi, E.P., and Rapp, R.P. (1989) Inclusion/host relations involving accessory
718 minerals in high-grade metamorphic and anatectic rocks. *Contributions to Mineralogy
719 and Petrology*, 101, 220-231.
- 720 Williams, M.L., Jercinovic, M.J., Harlov, D.E., Budzyń, B., and Hetherington, C.J. (2011)
721 Resetting monazite ages during fluid-related alteration. *Chemical Geology*, 283, 218-225.
- 722 Williams, M.L., Jercinovic, M.J., and Hetherington, C.J. (2007) Microprobe Monazite
723 Geochronology: Understanding geological processes by integrating composition and
724 chronology. *Annual Reviews - Earth and Planetary Sciences*, 35, 137-175.

- 725 Wolf, M.B., and London, D. (1994) Apatite dissolution into peraluminous haplogranitic melts:
726 An experimental study of solubilities and mechanisms. *Geochimica et Cosmochimica*
727 *Acta*, 58, 4127-4145.
- 728 -. (1995) Incongruent dissolution of REE- and Sr-rich apatite in peraluminous granitic liquids:
729 Differential apatite, monazite, and xenotime solubilities during anatexis. *American*
730 *Mineralogist*, 80, 765-775.
- 731 Yeo, G.M., and Delaney, G. (2007) The Wollaston Supergroup, stratigraphy and metallogeny of
732 a Paleoproterozoic Wilson cycle in the Trans-Hudson Orogen, Saskatchewan. In C.W.
733 Jefferson, and G. Delaney, Eds. EXTECH IV: Geology and Uranium EXploration
734 TECHnology of the Proterozoic Athabasca Basin, Saskatchewan and Alberta, p. 89-117.
735 Geological Survey of Canada Bulletin 588.
- 736
- 737
- 738

Figure Captions

739
740

741 Figure 1. Regional and local geology of the Kulyk Lake monazite-apatite-ilmenite REE
742 occurrences relative to the major lithotectonic domains comprising the Hearne Province in
743 northern Saskatchewan. A) Regional lithotectonic subdivisions identified within the Hearne
744 Domain of the Western Churchill Province in Saskatchewan (Bickford et al., 1990; Hoffman,
745 1990). B) Local geology adjacent to Kulyk Lake showing the location of the monazite-apatite-
746 Fe(Ti)-oxide mineralization relative to regional amphibolite-facies paragneiss and syn- to post-
747 tectonic granite and pegmatite bodies.

748 Figure 2. A) Detail geology of the Kulyk Lake monazite-apatite-Fe(Ti)-oxide occurrence. The
749 mineralization occurs in association with an aplitic leucogranite dyke which is in turn enclosed
750 by a locally pegmatite leucogranite dyke. B) A polished slab of sample MMKJG037 showing
751 the distribution of granoblastic monazite-rich and apatite-rich zones within the mineralized zone.
752 Dark clots of titanomagnetite are heterogeneously distributed. The area of the occurrence is
753 overprinted by an earthy hematite alteration that appears to have infiltrated along fracture planes.
754 C) portion of a polished thin section obtained from MMKJG037 showing the granoblastic nature
755 of monazite and apatite with titanomagnetite forming either interstitial to the phosphates or as
756 larger poikilitic grains enclosing apatite. Zircon occurs as a ubiquitous accessory mineral and is
757 included within all of the other major minerals in the rock.

758 Figure 3. A) Reflected light image showing grain boundary relationship between monazite,
759 apatite, titanomagnetite (T-mag), and zircon. Apatite locally forms euhedral to subhedral
760 hexagonal grains. Zircon grains included in apatite locally display well-developed radial
761 fractures typically associated with positive volume change in zircon during accumulation of

762 radiation damage (metamictization). This image also shows the interstitial nature of
763 titanomagnetite which locally forms thin meniscuses between apatite and monazite. Exsolution
764 of rutile (Rt) and abundant micron-scale ilmenite are also visible within the titanomagnetite host.
765 B) Cathodoluminescence image of a portion of a single apatite grains. Arrows point to dark-CL
766 healed fractures that are not visible in optical or BSE images. A dark-CL network of potentially
767 recrystallized apatite also envelopes occluded zircon grains and those decorating the grain
768 boundary with the adjacent grain below.

769 Figure 4. Reflected light photomicrograph mosaic showing details of a zircon-rich portion of
770 monazite-apatite-Fe(Ti)-oxide zone. Zircon occurs primarily along grain boundaries or at triple
771 junctions in the monazite-apatite aggregate. A lower proportion of zircon grains occur included
772 within the cores of apatite and rarely within monazite grains. A large fraction of the zircon
773 displays higher reflectance overgrowths.

774 Figure 5. Backscattered electron (BSE) image of a monazite-rich portion of the occurrence.
775 BSE-imaging revealed the presence of three distinct compositional domains: 1) bright-BSE
776 cores; 2) dark-BSE oscillatory zoned core domains, and; 3) uniform-BSE overgrowths.

777 Figure 6. Trace-element maps measured by LA-ICP-MS showing the semi-quantitative
778 concentrations of U, V, As, Th/U and $(La/Yb)_{CN}$ in monazite grains 1 and 2. In both case the
779 monazite grain is surrounded by apatite. Hot colours correspond to high concentrations whereas
780 cold colours correspond to low concentrations. Semi-quantitative concentration scale is given
781 for each element. Low-U cores contains domains with anomalously high As and V
782 concentrations in addition to discrete high Th/U domains and minor $(La/Yb)_{CN}$ zoning.

783 Figure 7. Reflected light live video image from the laser (background) with superimposed semi-
784 transparent trace element map showing the distribution of vanadium. The sample was polished
785 with 3 μm diamond past after raster mapping to remove most of the laser ablation damage (some
786 is still visible). Dark circles are craters left by ablations with 13 μm and 17 μm diameter spot
787 used for U-Pb geochronology. Red circles are the locations of targets for full trace element
788 quantification.

789 Figure 8. Chondrite-normalized REE patterns for monazite grains 1, 2, and 3 with data for
790 Trebilcock and 44069 standards for comparison. Slightly higher Er value is probably a result of
791 a small $^{150}(\text{Nd}+\text{Sm})^{16}\text{O}^+$ interference on ^{166}Er . The data were calculated using Nd as an internal
792 standard at concentrations previously determined by EPMA. The Kulyk Lake monazite displays
793 very high LREE/HREE fractionation with $(\text{La}/\text{Yb})_{\text{CN}}$ values > 1000 .

794 Figure 9. Histogram and probably density plot of $^{207}\text{Pb}/^{206}\text{Pb}$ ages for inherited components in
795 monazite grains 1, 2, and 3. The provenance of the inherited domains is dominated by
796 Paleoproterozoic ages with major peaks at 1880 Ma and 2150 Ma and a broad spectrum of ages
797 centered at about 2050 Ma.

798 Figure 10. Compilation of trace element compositional zoning for V, Th/U, and Mo in monazite
799 grain 3 with superimposed $^{207}\text{Pb}/^{206}\text{Pb}$ ages measured using 17 μm diameter craters. Absolute 2σ
800 errors (not shown for clarity) are 15 to 17 Ma (i.e., $\sim 1\%$). There is a close correspondence
801 between compositional zoning and $^{207}\text{Pb}/^{206}\text{Pb}$ age with Mo-enriched domains preserving 2020
802 Ma to 2150 Ma ages whereas patchy low Th/U domains are 1870 Ma to 1900 Ma. The resorbed
803 low-V and low-Mo nucleus preserves older Paleoproterozoic ages and is interpreted to be
804 detrital.

805 Figure 11. Conventional Concordia diagrams showing the results of in-situ U-Pb geochronology
806 applied to monazite in the monazite-apatite-ilmenite vein (A, B) and in the aplitic host to the
807 vein (C,D). Black squares are the absolute positions of the measured ratios which are used to
808 help identify data clusters. Both samples contain higher-U overgrowths that crystallized at 1828
809 \pm 6 Ma. Both rocks were also affected by a younger thermal resetting event between 1770 Ma to
810 1790 Ma.

811

Table 1. LA-ICP-MS trace element quality control on GSE-1G

Analyte	Mean (ppm)	GSE-1G		Average D.L. (ppm)	
		<i>1σ</i>	Ref. value (ppm)		
⁴⁴ Ca	52750	2100	52887	2140	890
⁵¹ V	446	20	440	20	1.39
⁷⁵ As	392	14	260	90	8.72
⁸⁹ Y	415	40	410	30	0.16
⁹³ Nb	441	11	420	40	0.18
⁹⁸ Mo	401	11	390	30	0.34
¹³⁷ Ba	364	11	427	5	0.21
¹³⁹ La	391	11	392	4	2.01
¹⁴⁰ Ce	411	11	414	4	0.81
¹⁴¹ Pr	464	27	460	10	1.10
¹⁴⁶ Nd I.S.			453		
¹⁴⁷ Sm	489	42	488	5	0.35
¹⁵³ Eu	411	9	410	20	0.06
¹⁵⁷ Gd	527	18	490	70	0.48
¹⁵⁹ Tb	511	12	480	20	0.05
¹⁶³ Dy	550	14	524	6	0.12
¹⁶⁵ Ho	514	53	489	6	0.02
¹⁶⁶ Er	586	14	595	6	0.04
¹⁶⁹ Tm	531	38	500	20	0.01
¹⁷³ Yb	535	13	520	5	0.09
¹⁷⁵ Lu	538	55	518	6	0.01
²⁰⁸ Pb	382	10	378	12	0.36
²³² Th	387	24	380	20	0.04
²³⁸ U	431	11	420	30	0.03

812

813

Table 2. EPMA major element chemistry of BSE imaged compositional domains

El. Wt%	Cores - Bright BSE oscillatory zones		Cores - Dark BSE oscillatory zones		Overgrowths	
	Mean ($n = 5$)	1σ	Mean ($n = 7$)	1σ	Mean ($n = 7$)	1σ
P	13.2	0.2	13.3	0.1	12.8	0.06
Si	0.27	0.0	0.22	0.0	0.49	0.05
Ca	0.56	0.1	0.55	0.0	0.41	0.08
La	14.0	0.3	14.3	0.3	13.9	0.39
Ce	27.1	0.4	27.1	0.5	27.2	0.28
Pr	2.20	0.1	2.21	0.1	2.28	0.17
Nd	9.08	0.2	9.04	0.3	9.05	0.24
Y	0.27	0.2	0.23	0.2	0.20	0.21
Th	3.32	0.5	2.86	0.4	4.41	0.46

814

815

Table 3. Monazite grain1, LA-ICP-MS trace element data

Analysis#	Map1, High-V cores				Map 1, higher-U uniform overgrowths				
	1	2	3	4	1	2	3	4	5
⁴⁴ Ca	5140	4850	4560	5900	3390	3760	3440	3510	3600
⁵¹ V	310	277	274	252	60	110	107	132	103
⁷⁵ As*	1214	1167	1607	1265	1034	1145	969	1109	1092
⁸⁹ Y	5129	4971	4190	4830	4660	4459	4850	4340	4746
⁹³ Nb	<0.18	<0.18	<0.18	0.25	<0.18	0.22	<0.18	0.19	<0.18
⁹⁸ Mo	<0.34	<0.34	<0.34	0.34	<0.34	0.32	0.81	0.67	0.49
¹³⁷ Ba	3.01	5.09	2.53	29.0	0.67	4.10	0.51	0.57	0.01
¹³⁹ La	158900	159200	150800	148300	123200	137600	135700	141600	137000
¹⁴⁰ Ce	299500	296200	293400	291200	258000	273900	269100	282300	276600
¹⁴¹ Pr	30500	29920	29830	29970	28140	29710	28470	29540	28720
¹⁴⁶ Nd I.S.	90000	90000	90000	90000	90000	90000	90000	90000	90000
¹⁴⁷ Sm	9940	9540	9580	9830	10680	10160	10360	9840	10310
¹⁵³ Eu	1057	1054	998	1063	1129	1105	1094	1049	1122
¹⁵⁷ Gd	6059	5840	5680	5792	6040	5760	6070	5550	5910
¹⁵⁹ Tb	434	414	380	414	426	409	435	390	418
¹⁶³ Dy	1552	1486	1330	1439	1479	1386	1527	1354	1476
¹⁶⁵ Ho	201	191	167	188	181	178	186	172	186
¹⁶⁶ Er	360	349	294	338	306	297	322	296	319
¹⁶⁹ Tm	29.4	28.4	23.0	27.2	22.7	22.6	25.2	23.2	23.5
¹⁷³ Yb	113	105	84.8	103	81.8	81.9	88.1	86.5	87.4
¹⁷⁵ Lu	13.0	13.0	16.5	17.0	19.1	24.0	23.2	27.2	24.3
²⁰⁸ Pb	4230	3680	6720	7480	3652	6440	4890	6410	6420
²³² Th	26110	22720	39800	44500	23240	36520	35000	38900	39510
²³⁸ U	78	79	96	96	126	159	153	171	156
Eu/Eu*	0.25	0.26	0.25	0.26	0.26	0.26	0.25	0.26	0.26
(La/Yb) _{CN}	960	1029	1208	983	1023	1141	1046	1112	1065
Th/U	335	289	415	464	184	230	229	228	254

816 Values in ppm

817

Table 4. Monazite grain2, LA-ICP-MS trace element data

Analysis#	Map2, High-Vanadium cores			Map 2, higher-U uniform overgrowths		
	1	2	3	1	2	3
⁴⁴ Ca	4650	4160	3880	4200	3930	4260
⁵¹ V	334	240	277	107	112	111
⁷⁵ As*	1758	1516	1656	994	961	995
⁸⁹ Y	3855	4220	4042	3909	3903	3939
⁹³ Nb	<0.18	0.93	<0.18	<0.18	0.23	<0.18
⁹⁸ Mo	<0.34	0.42	<0.34	0.61	0.56	0.52
¹³⁷ Ba	62.8	21.4	0.33	0.46	0.21	0.28
¹³⁹ La	147600	149000	152300	143900	145600	145500
¹⁴⁰ Ce	296300	283100	294100	290800	286100	286600
¹⁴¹ Pr	29940	29310	29660	29530	29540	29300
¹⁴⁶ Nd I.S.	90000	90000	90000	90000	90000	90000
¹⁴⁷ Sm	9720	9630	9670	9730	9490	9590
¹⁵³ Eu	1000	988	995	979	968	967
¹⁵⁷ Gd	5310	5358	5218	5123	5137	5123
¹⁵⁹ Tb	374.1	383.1	366	357.7	349.4	359.8
¹⁶³ Dy	1247	1349	1280	1203	1216	1231
¹⁶⁵ Ho	157	173	159	154	152	153
¹⁶⁶ Er	268	301	273	263	265	269
¹⁶⁹ Tm	20.7	23.8	20.1	20.3	20.6	20.8
¹⁷³ Yb	71.2	88.7	74.1	75.0	77.6	74.3
¹⁷⁵ Lu	6.07	8.22	6.33	6.74	6.9	6.84
²⁰⁸ Pb	8420	8670	8100	4340	4490	4890
²³² Th	49300	55100	50200	27170	27850	30620
²³⁸ U	97	107	91	127	136	143
Eu/Eu*	0.25	0.25	0.25	0.25	0.25	0.25
(La/Yb) _{CN}	1408	1141	1396	1303	1275	1330
Th/U	507	515	549	215	206	214

818 Values in ppm

819

Table 5. Monazite grain3, LA-ICP-MS trace element data

Analyte	Map 3, high-Mo core domains					Map 3, low Th/U			Low-V
	Core	Core-1	Core-2	Core-3	Core-4	Ogl	Ogl-1	Ogl-2	
⁴⁴ Ca	7620	8050	5690	5490	6110	5320	5600	4880	5390
⁵¹ V	151	159	148	150	139	181	185	189	120
⁷⁵ As*	1153	1118	1052	1090	978	1062	1022	974	1405
⁸⁹ Y	4239	4241	4151	4124	4165	4207	4262	4015	4108
⁹³ Nb	0.46	0.66	0.47	0.34	0.35	0.50	0.44	0.46	0.18
⁹⁸ Mo	9.05	9.27	4.98	4.40	4.20	3.67	3.28	2.59	<0.34
¹³⁷ Ba	1.15	2.40	7.70	7.10	0.64	1.49	0.41	0.52	0.42
¹³⁹ La	15640	15760	15670	15520	15450	158600	15690	15960	15610
¹⁴⁰ Ce	29900	30310	29640	29530	29720	301900	29970	30080	29640
¹⁴¹ Pr	30580	30600	30180	30090	30310	30700	30600	30300	30620
¹⁴⁶ Nd I.S.	90000	90000	90000	90000	90000	90000	90000	90000	90000
¹⁴⁷ Sm	9280	9520	9460	9380	9420	9490	9460	9330	9350
¹⁵³ Eu	972	988	983	995	995	999	979	923	987
¹⁵⁷ Gd	6252	6126	6175	5997	5965	5954	5983	5767	6230
¹⁵⁹ Tb	398	394	392	395	389	390	393	372	398
¹⁶³ Dy	1325	1322	1308	1312	1323	1334	1336	1248	1294
¹⁶⁵ Ho	167	164	163	164	166	168	170	156	161
¹⁶⁶ Er	293	284	284	287	286	296	300	277	274
¹⁶⁹ Tm	23.7	23.3	22.4	23.1	21.8	23.7	24.1	22.2	21.0
¹⁷³ Yb	87.6	90.3	84.9	85.2	84.3	90.2	92.5	84	75.8
¹⁷⁵ Lu	8.22	8.24	8	7.54	7.79	8.24	8.56	7.65	6.71
²⁰⁸ Pb	8400	8160	7930	7880	7640	8300	8030	8320	8380
²³² Th	49730	48520	47160	45680	45370	49080	48180	49480	50010
²³⁸ U	179	177	178	177	175	326	329	247	134
Eu/Eu*	0.25	0.25	0.25	0.25	0.25	0.25	0.25	0.24	0.25
(La/Yb) _c	1213	1186	1254	1237	1245	1194	1152	1291	1399
Th/U	278	275	265	258	259	151	146	200	374

820 Values in ppm

821

Table 6. LA-ICP-MS trace elements of monazite standards

Analyte	Trebilcock (<i>n</i> = 5)		44069 (<i>n</i> = 4)	
	Average	1 σ	Average	1 σ
⁴⁴ Ca	12548	2015	4160	239
⁵¹ V	<1.39	-	2.80	0.12
⁷⁵ As*	589	10	470	5
⁸⁹ Y	22520	2615	15990	679
⁹³ Nb	<0.18	-	<0.18	-
⁹⁸ Mo	<0.34	-	<0.34	-
¹³⁷ Ba	<0.21	-	<0.21	-
¹³⁹ La	73600	5616	84925	2076
¹⁴⁰ Ce	186900	8472	173750	592
¹⁴¹ Pr	24806	470	21938	244
¹⁴⁶ Nd I.S.	100000		98000	
¹⁴⁷ Sm	36108	1099	16483	306
¹⁵³ Eu	173	27	1996	95
¹⁵⁷ Gd	23854	1338	12535	539
¹⁵⁹ Tb	2712	206	1372	42
¹⁶³ Dy	9164	886	5788	185
¹⁶⁵ Ho	813	93	705	14
¹⁶⁶ Er	1197	162	1148	44
¹⁶⁹ Tm	101	15	85.2	8
¹⁷³ Yb	407	57	294	41
¹⁷⁵ Lu	32.3	5	24.2	4
²⁰⁸ Pb	3728	559	579	37
²³² Th	162140	24559	17173	1301
²³⁸ U	5971	897	1920	262
Eu/Eu*	0.01	0	0.28	0
(La/Yb) _{CN}	123	20	196	33
Th/U	27	2	9	2

822 Values in ppm

823

Table 7. Results of in-situ LA-ICP-MS U-Pb monazite geochronology

Comments	%Pb*	$^{207}\text{Pb}/^{235}\text{U}$	2 σ	$^{206}\text{Pb}/^{238}\text{U}$	2 σ	Err. corr.	$^{207}\text{Pb}/^{206}\text{Pb}$ age (Ma)	2SE	%Disc
<i>Host aplite dyke – thermal resetting</i>									
Mnz5b	100.0	4.80	0.08	0.3193	0.0036	0.41	1782	15	-0.2
Mnz2b	100.0	4.81	0.08	0.3184	0.0035	0.68	1791	12	0.5
Mnz15-core	99.8	4.81	0.09	0.3191	0.0060	0.58	1792	15	0.1
Mnz4	99.8	4.85	0.09	0.3200	0.0048	0.42	1798	15	0.4
<i>Host aplite dyke – crystallization age</i>									
Mnz3b	99.8	5.04	0.08	0.3264	0.0041	0.45	1829	11	0.4
Mnz17a	99.9	5.04	0.12	0.3263	0.0068	0.59	1826	20	0.2
Mnz15-ovrgr	100.0	5.05	0.10	0.3269	0.0055	0.57	1814	15	-0.7
Mnz22	100.1	5.06	0.08	0.3279	0.0045	0.49	1821	11	-0.4
<i>LA-ICP-MS map-guided spots</i>									
Map1_core-1	100.1	5.68	0.11	0.3468	0.0042	0.19	1925	21	0.3
Map1_core-2	99.9	5.87	0.11	0.3512	0.0046	0.42	1963	19	1.2
Map1_core-3	99.9	6.03	0.11	0.3587	0.0046	0.55	1979	15	0.2
Map1_core-4	99.9	5.36	0.01	0.3372	0.0046	0.36	1873	21	0.1
Map1_core-5	99.6	5.32	0.09	0.3347	0.0040	0.33	1878	17	1.0
Map2_core-1*	97.9	4.77	0.11	0.3141	0.0048	0.98	1831	26	-2.6
Map2_core-2*	98.7	5.39	0.13	0.3358	0.0051	0.96	1912	23	2.2
Map2_core-3*	98.9	5.20	0.12	0.3292	0.0051	0.97	1886	23	2.3
Map3_highMo-1*	97.5	5.20	0.11	0.3275	0.0046	0.97	1895	27	0.9
Map3_highMo-2*	97.5	5.13	0.10	0.3245	0.0042	0.98	1876	24	1.4
Map3_highMo-3*	98.1	5.20	0.10	0.3294	0.0045	0.96	1894	24	1.2
Map3_highMo-4*	98.3	5.26	0.12	0.3304	0.0050	0.97	1905	26	3.0
Map3_highMo-5*	98.7	5.39	0.11	0.3328	0.0045	0.96	1919	24	3.1
Map3_highMo-6*	98.6	5.17	0.10	0.3273	0.0045	0.95	1890	24	3.4
Map3_lowV_core*	94.6	4.90	0.09	0.3144	0.0043	0.99	1847	16	2.5
Map3_lowV_core*	94.6	4.91	0.09	0.3139	0.0045	0.99	1851	15	3.8
Map3_ovrgr-1	100.0	5.60	0.07	0.3442	0.0035	0.45	1897	14	-0.5
Map3_ovrgr-2	100.0	5.45	0.06	0.3399	0.0037	0.48	1870	14	-0.9
Map3_ovrgr-3	99.7	5.41	0.06	0.3351	0.0035	0.30	1883	13	1.1
Map3_ovrgr-4	99.9	5.46	0.07	0.3408	0.0038	0.61	1880	15	-0.5
Map3_ovrgr-5	99.8	5.56	0.06	0.3436	0.0037	0.24	1889	15	-0.9
Map3_ovrgr-6	99.9	5.59	0.07	0.3446	0.0038	0.31	1875	12	-1.8
<i>BSE-guided spots – thermal resetting</i>									
Ovrgr	100.0	4.72	0.11	0.3152	0.0071	0.60	1780	23	0.9
Oscll core	100.0	4.73	0.34	0.3150	0.0063	0.35	1763	69	-0.1
Ovrgr	100.0	4.65	0.13	0.3126	0.0063	0.36	1794	28	2.3
Ovrgr	99.7	4.69	0.12	0.3164	0.0050	0.42	1776	24	0.2
Ovrgr	100.0	4.76	0.14	0.3168	0.0049	0.39	1772	27	-0.1
<i>BSE-guided spots – crystallization age</i>									
Ovrgr	99.9	5.08	0.12	0.3287	0.0055	0.50	1829	18	-0.3
Ovrgr	100.0	5.11	0.16	0.3293	0.0049	0.34	1809	32	-1.5
Ovrgr	99.9	5.10	0.25	0.3298	0.0060	0.13	1839	41	0.1
Ovrgr	100.0	5.09	0.17	0.3299	0.0067	0.56	1832	28	-0.3
Ovrgr	100.0	5.01	0.13	0.3278	0.0067	0.46	1846	27	1.1

824 * analyses corrected for common-Pb using the Andersen (2002) correction routine.

Table 8. Results of in-situ LA-ICP-MS U-Pb zircon geochronology

Comments	%Pb*	$^{207}\text{Pb}/$ ^{235}U	2σ	$^{206}\text{Pb}/$ ^{238}U	2σ	Err. corr	$^{207}\text{Pb}/^{206}\text{Pb}$ age (Ma)	2σ	%Disc
z-30	100.6	4.82	0.13	0.3198	0.0110	0.75	1797	26	0.5
z-20-2	99.3	4.83	0.10	0.3176	0.0081	0.52	1797	31	1.1
z-12	99.6	4.96	0.07	0.3138	0.0083	0.10	1871	19	5.8
z-13	99.6	4.91	0.11	0.3089	0.0100	0.87	1871	47	7.3
z-28	98.7	4.65	0.09	0.2932	0.0083	0.56	1848	30	10.3
z-11	98.7	4.74	0.08	0.2950	0.0083	0.65	1900	22	12.3
z-3-1	97.2	4.61	0.14	0.2866	0.0100	0.75	1906	28	14.8
z-18	98.2	4.38	0.09	0.2633	0.0077	0.70	1961	27	23.2
z-1	96.7	4.40	0.08	0.2632	0.0080	0.57	1971	28	23.6
z-14	97.0	4.50	0.07	0.2638	0.0070	0.47	1998	26	24.5
z-27	96.5	4.36	0.09	0.2609	0.0084	0.76	1979	26	24.5
z-25	96.8	6.29	0.21	0.3160	0.0130	0.92	2345	20	24.6
z-15	96.7	4.37	0.11	0.2611	0.0100	0.62	1989	30	24.8
z-8	97.0	4.28	0.09	0.2548	0.0068	0.39	1972	34	25.8
z-26-2	96.7	3.75	0.10	0.2326	0.0075	0.78	1897	29	28.9
z-17	96.6	3.96	0.12	0.2381	0.0092	0.81	1943	31	29.2
z-6	96.4	4.00	0.09	0.2382	0.0065	0.60	1971	30	30.1
z-3-2	97.2	4.03	0.12	0.2349	0.0081	0.62	2049	42	33.6
z-8b	97.0	4.07	0.08	0.2344	0.0071	0.55	2051	37	33.8

825

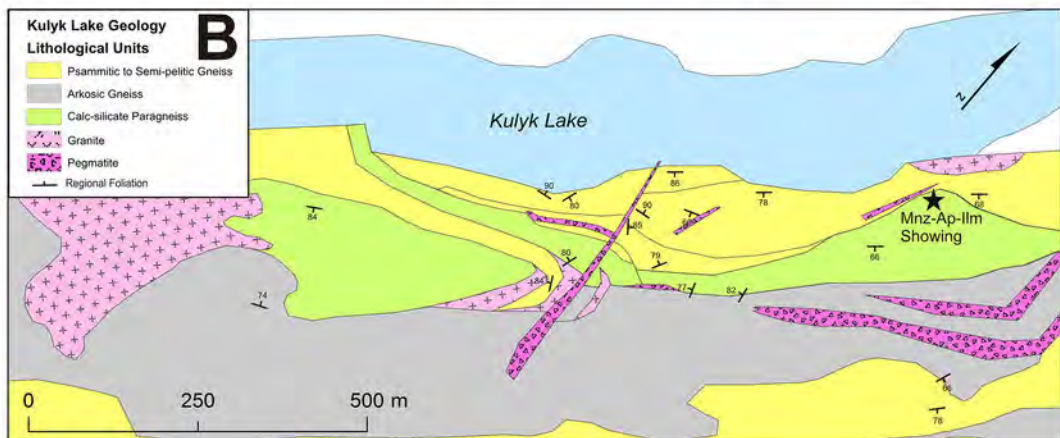
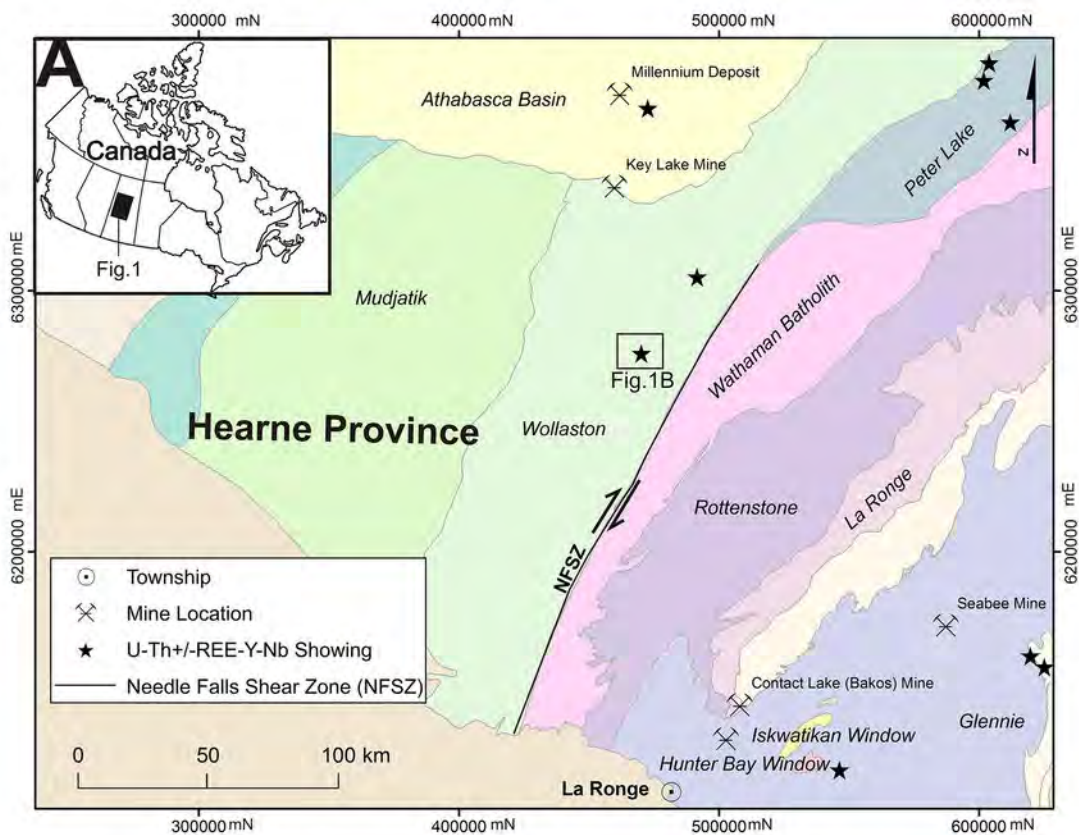
826

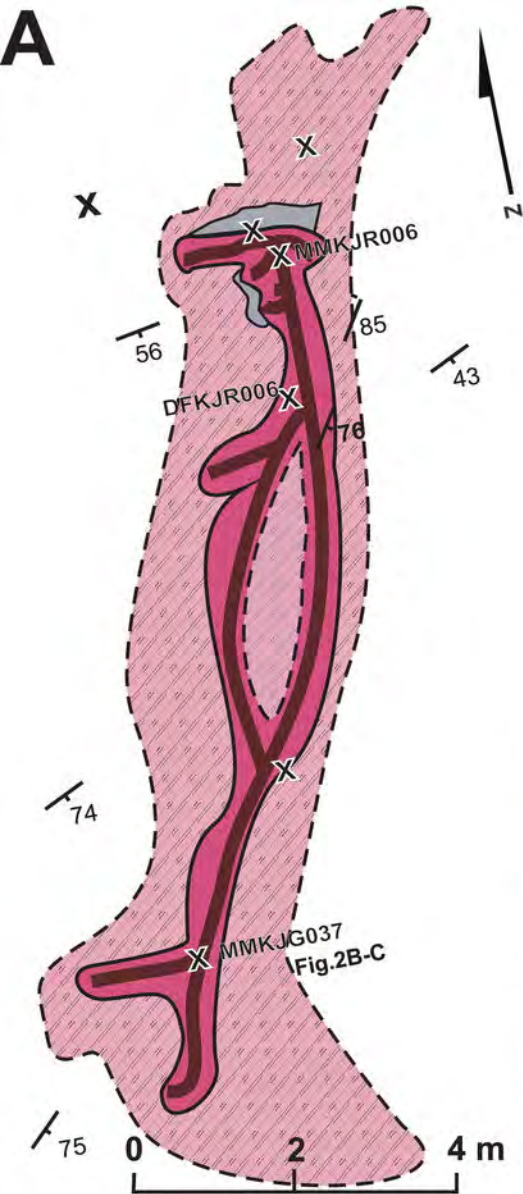
Table 9. Summary of in-situ LA-MC-ICP-MS Sm-Nd isotope data

Spot	$^{147}\text{Sm}/^{144}\text{Nd}$	2S.E.	$^{143}\text{Nd}/^{144}\text{Nd}$	2S.E.	$^{145}\text{Nd}/^{144}\text{Nd}$	2S.E.	eNd(t)	\pm	T_{DM}
1.1	0.0584	0.0004	0.510732	0.000017	0.348444	0.000012	-4.73	0.73	2405
2.1	0.0579	0.0003	0.510719	0.000018	0.348433	0.000013	-4.86	0.72	2410
3.1	0.0570	0.0003	0.510703	0.000022	0.348446	0.000011	-4.96	0.83	2411
4.1	0.0598	0.0001	0.510774	0.000016	0.348427	0.000014	-4.22	0.63	2386
5.1	0.0582	0.0001	0.510715	0.000022	0.348431	0.000016	-5.00	0.78	2418
6.1	0.0588	0.0001	0.510759	0.000022	0.348444	0.000012	-4.28	0.79	2385
7.1	0.0575	0.0001	0.510719	0.000018	0.348424	0.000012	-4.77	0.66	2404
8.1	0.0577	0.0000	0.510717	0.000024	0.348448	0.000016	-4.85	0.81	2409
9.1	0.0572	0.0001	0.510725	0.000024	0.348438	0.000012	-4.59	0.83	2393
Spot	$^{147}\text{Sm}/^{144}\text{Nd}$	2S.E.	$^{143}\text{Nd}/^{144}\text{Nd}$	2S.E.	$^{145}\text{Nd}/^{144}\text{Nd}$	2S.E.			
Treb1.1	0.2217	0.0003	0.512616	0.000017	0.348444	0.000016			
Treb2.1	0.2208	0.0002	0.512581	0.000022	0.348440	0.000015			
Treb3.1	0.2208	0.0002	0.512613	0.000021	0.348448	0.000017			
Treb4.1	0.2211	0.0001	0.512621	0.000032	0.348441	0.000020			
Treb5.1	0.2214	0.0001	0.512592	0.000030	0.348430	0.000020			
Treb6.1	0.2203	0.0003	0.512600	0.000014	0.348432	0.000015			
Ref. value	0.2167	0.0125	0.512616	0.000011	0.348418	0.000008			

827

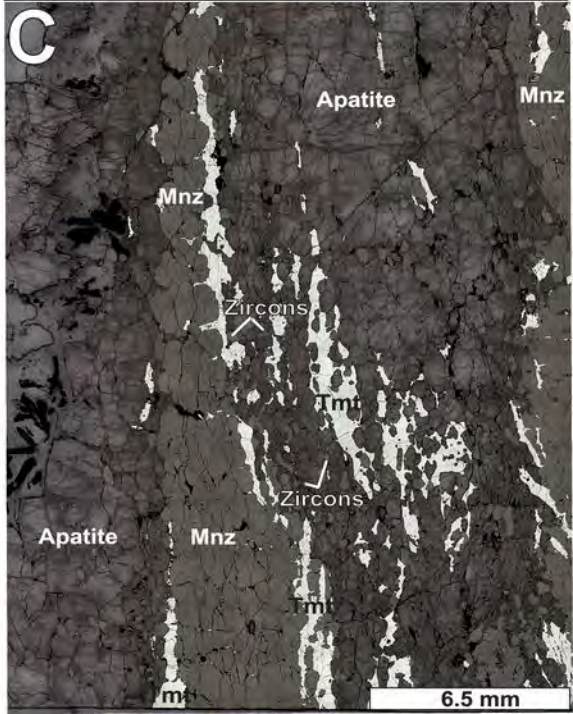
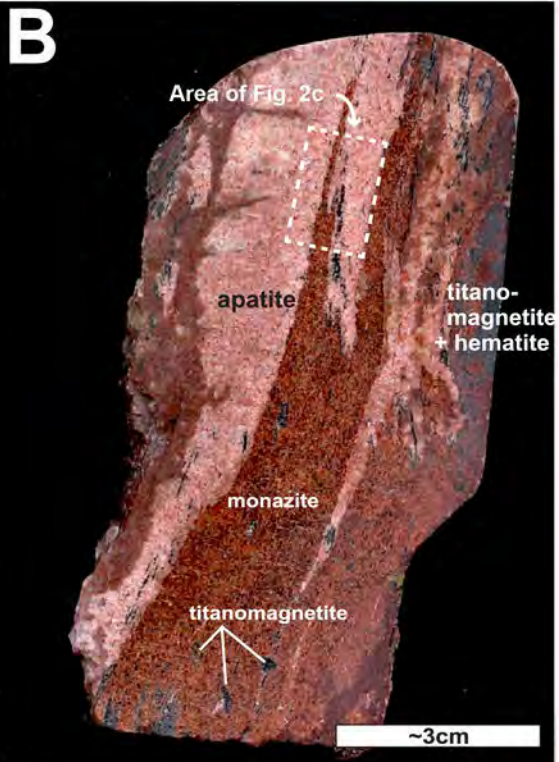
828

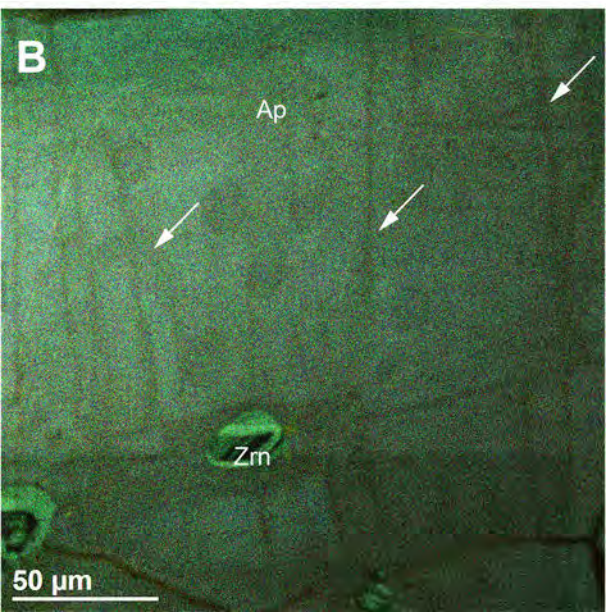
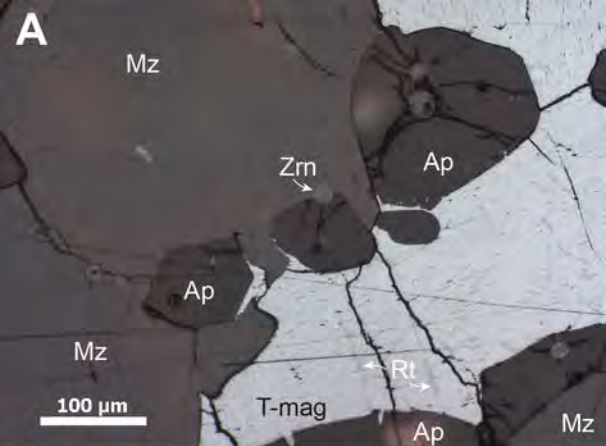


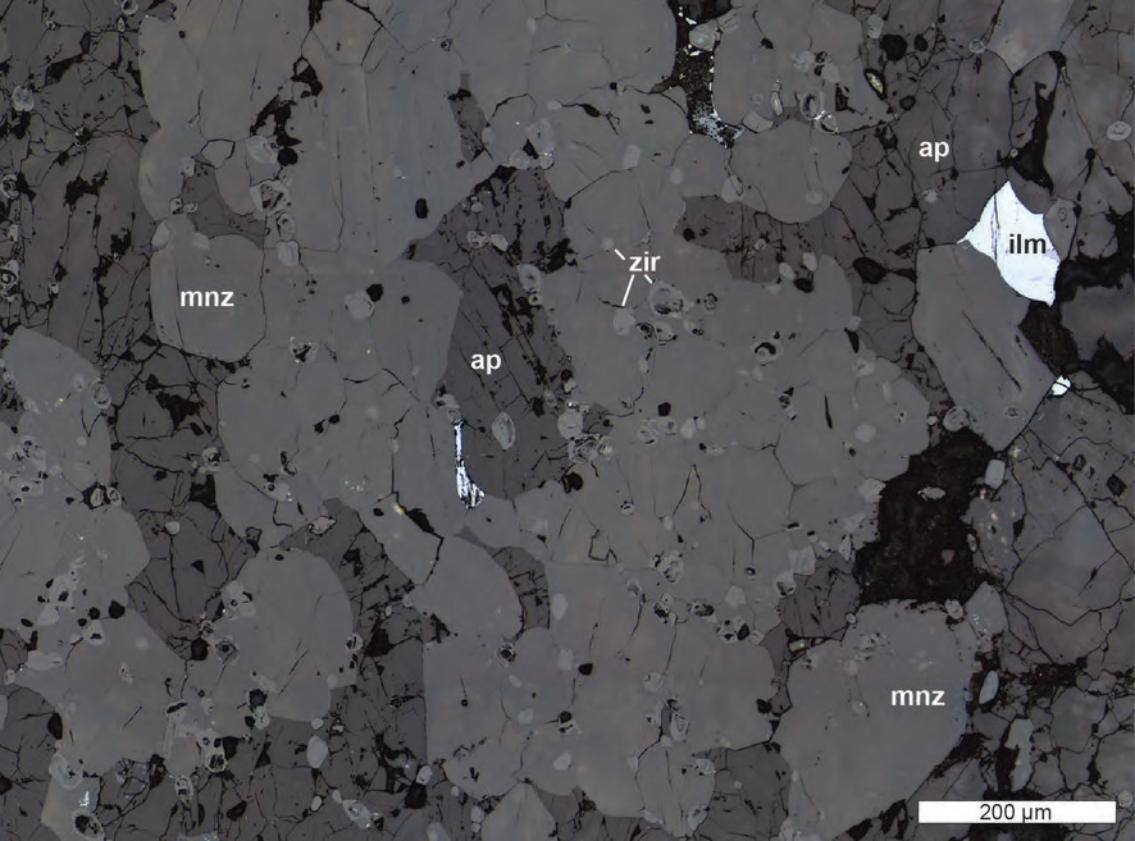


Lithological Units

- Calc-silicate Paragneiss
- Pegmatitic- to granitic- leucocratic dyke
- Aplitic leucocratic dyke
- Monazite-apatite-titanomagnetite mineralization
- Biotite-shist (metasomatic?) zone
- Regional Foliation







mnz

ap

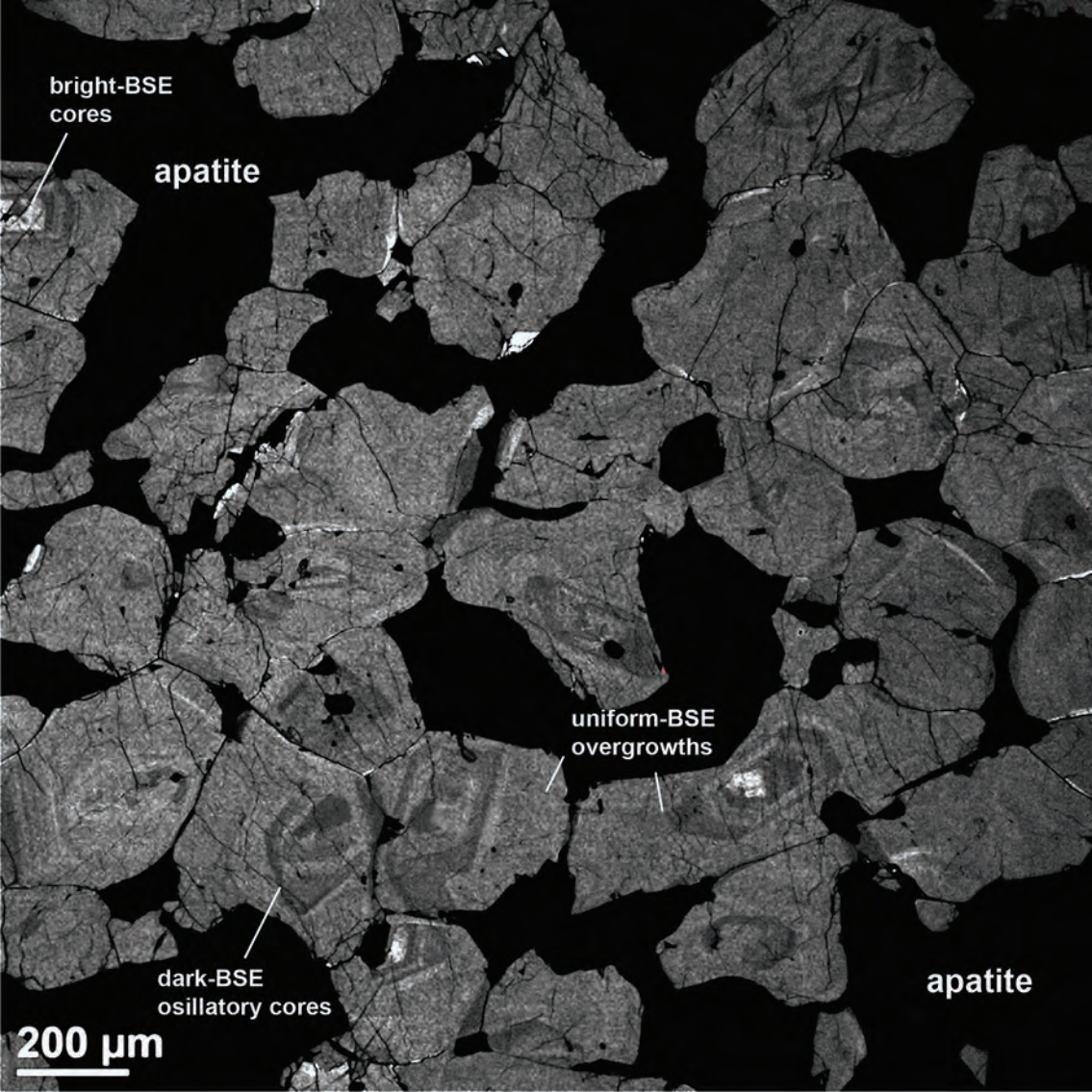
zir

ap

ilm

mnz

200 μ m



bright-BSE
cores

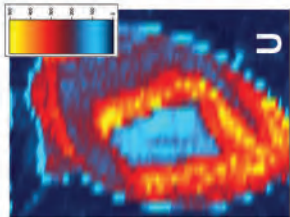
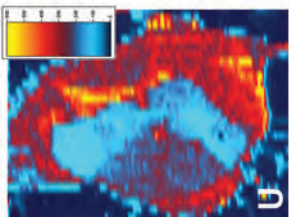
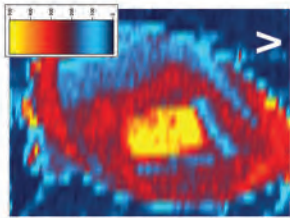
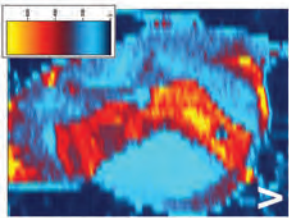
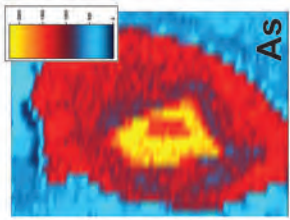
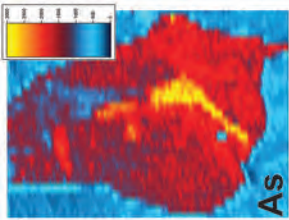
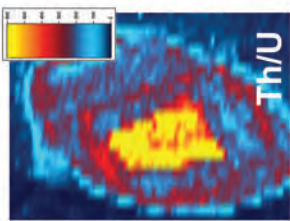
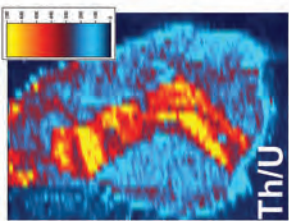
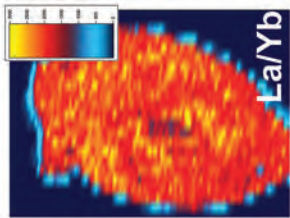
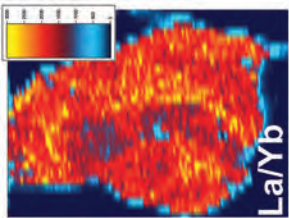
apatite

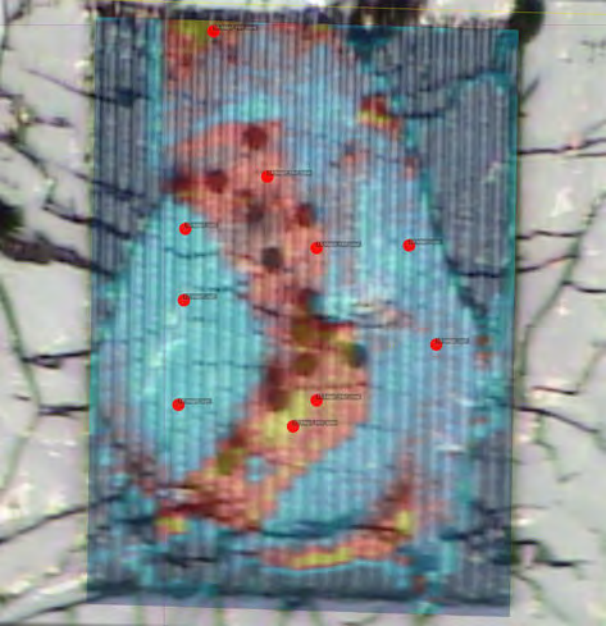
uniform-BSE
overgrowths

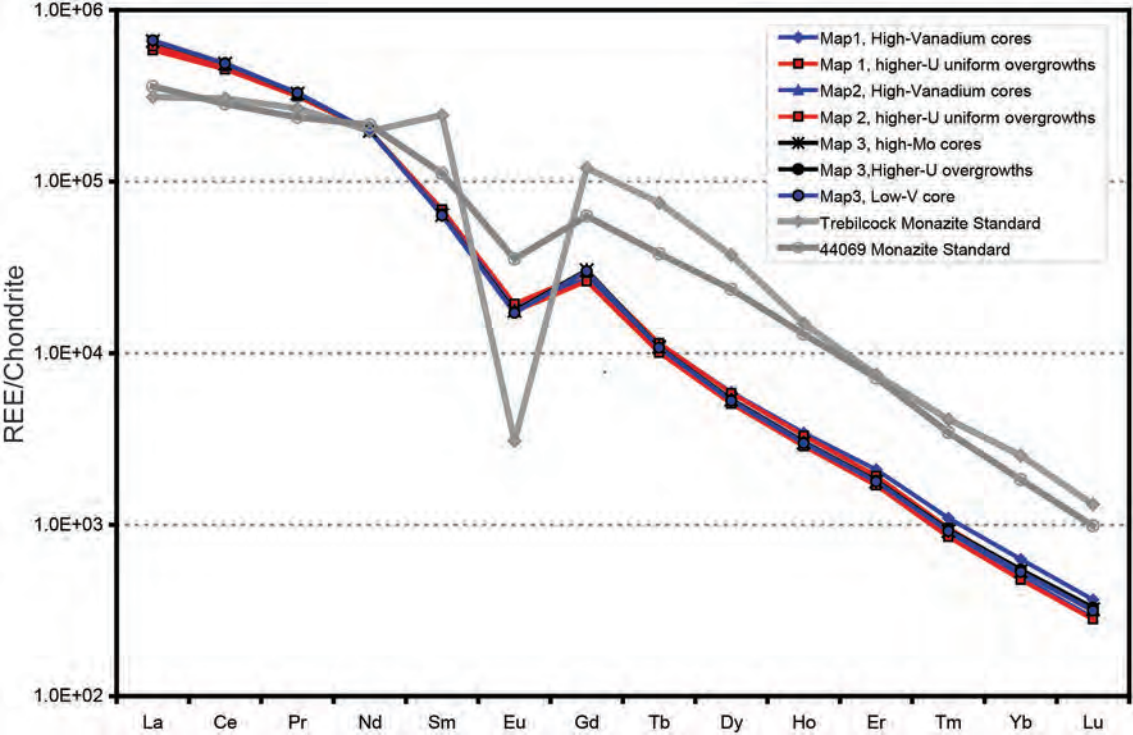
dark-BSE
osillatory cores

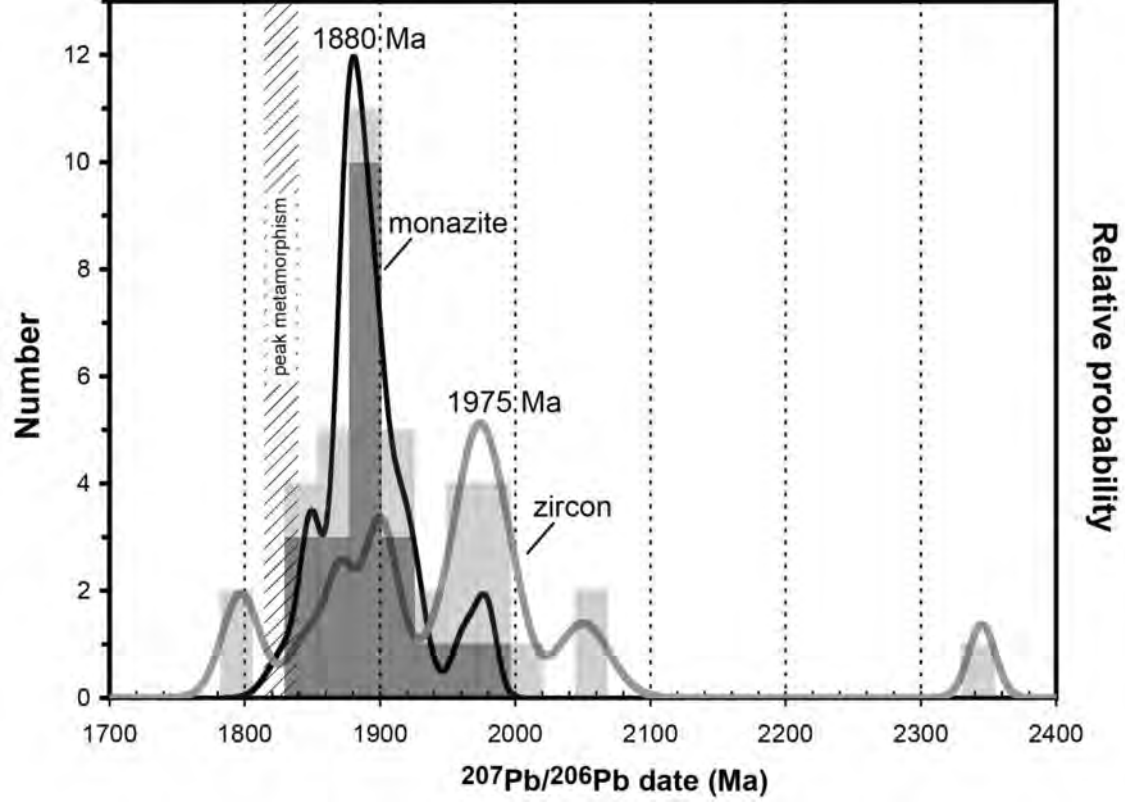
apatite

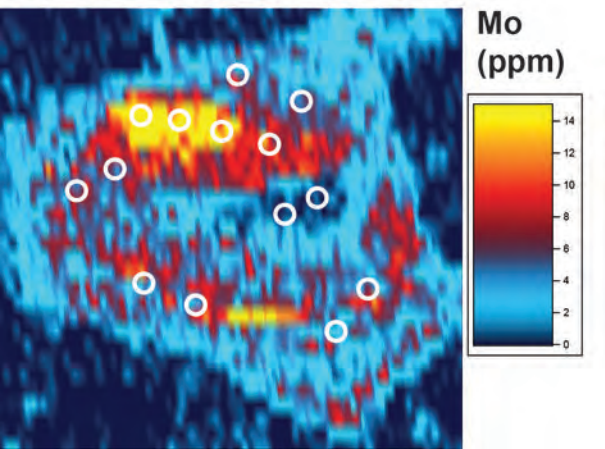
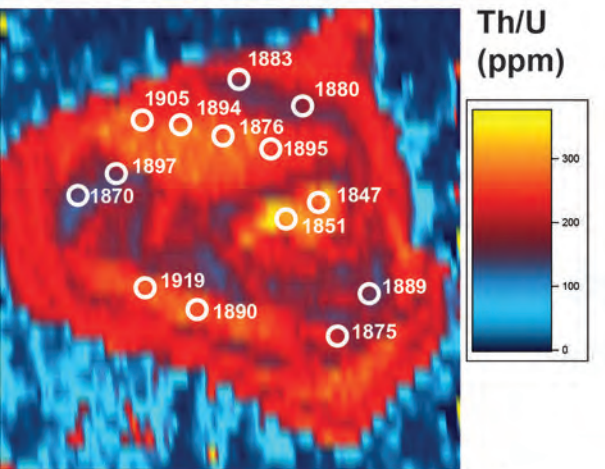
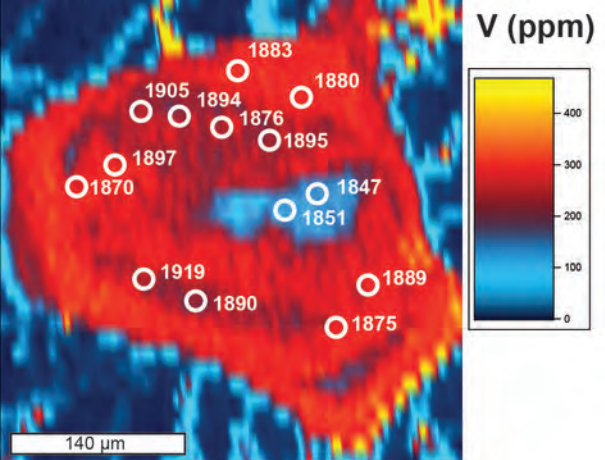
200 μm



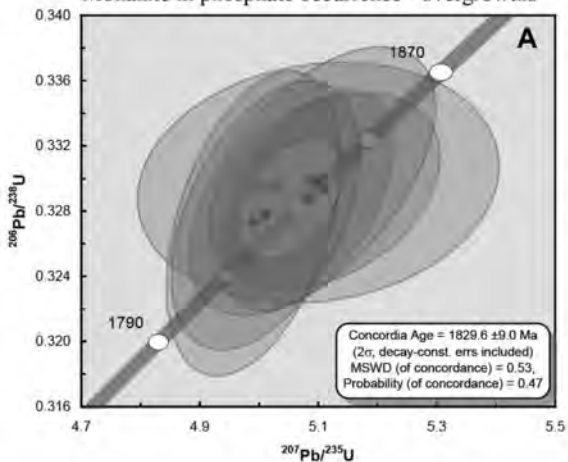




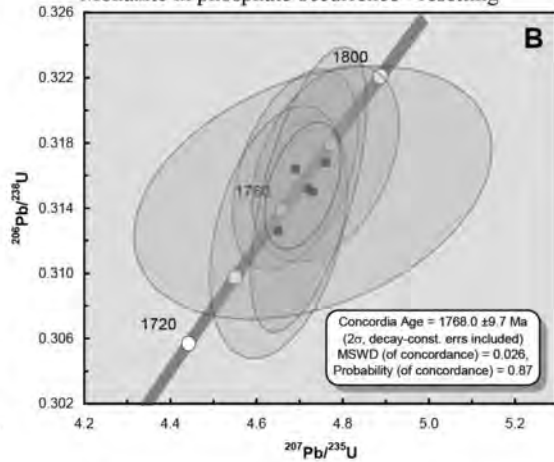




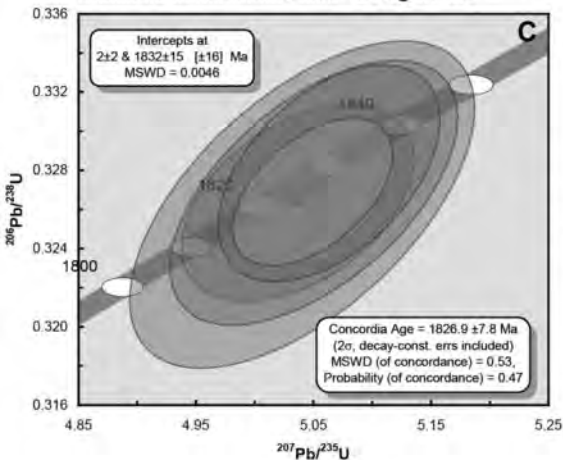
Monazite in phosphate occurrence - overgrowths



Monazite in phosphate occurrence - resetting



Monazite in monzonite host - overgrowths



Monazite in monzonite host - late thermal

